Evaluation and validation of a CFD solver adapted to atmospheric flows: Simulation of topography-induced waves

Norbert Rácz[1*]**, Gergely Kristóf**[1]**,** and **Tamás Weidinger**[2]

[1]*Department of Fluid Mechanics, Budapest University of Technology and Economics (BME),*
Bertalan L. u. 4-6, H-1111 Budapest, Hungary
E-mails: racz@ara.bme.hu; kristof@ara.bme.hu

[2]*Department of Meteorology, Eötvös Loránd University,*
P.O. Box 32, H-1518 Budapest, Hungary
weidi@caesar.elte.hu

*Corresponding author

(Manuscript received in final form December 15, 2012)

Abstract–Mountain wave phenomena have been simulated by using a well-known general purpose computational fluid dynamic (CFD) simulation system adapted to atmospheric flow modeling. Mesoscale effects have been taken into account with a novel approach based on a system of transformations and customized volume sources acting in the conservation and governing equations. Simulations of linear hydrostatic wave fields generated by a two-dimensional obstacle were carried out, and the resulting vertical velocity fields were compared against the corresponding analytic solution. Validation with laboratory experiments and full-scale atmospheric flows is a very important step toward the practical application of the method. Performance measures showed good correspondence with measured data concerning flow structures and wave pattern characteristics of non-hydrostatic and nonlinear mountain waves in low Reynolds number flows. For highly nonlinear atmospheric scale conditions, we reproduced the well-documented downslope windstorm at Boulder in January 1972, during which extreme weather conditions, with a wind speed of approximately 60 m s^{-1}, were measured close to the ground. The existence of the hydraulic jump, the strong descent of the stratospheric air, wave breaking regions, and the highly accelerated downslope wind were well reproduced by the model. Evaluation based on normalized mean square error (NMSE), fractional bias (FB), and predictions within a factor of two of observations (FAC2) show good model performance, however, due to the horizontal shift in the flow pattern, a less satisfactory hit rate and correlation value can be observed.

Key-words: complex terrain, gravity waves, CFD simulation, model validation, numerical weather prediction

1. Introduction

An extension of the physical model used in general purpose computational fluid dynamic (CFD) solvers has been developed recently in order to simulate mesoscale atmospheric flow phenomena in the same model with finely structured microscale flow around complex geometries (*Castro et al.*, 2008). We suggested a novel approach by utilizing a system of transformations and additional volume sources in the governing equations. Atmospheric stratification, adiabatic temperature change caused by vertical motion, baroclinicity, and Coriolis force are taken into account through this method (*Kristóf et al.,* 2009). The model uses only one single unstructured grid, and a uniform physical description for close- and far-field flow avoiding interpolation errors and model uncertainties due to model nesting. The authors intended purpose, furthermore, is to create a more general method, which is easy to implement in any CFD solver allowing programmable user defined volume sources in the governing equations. This new approach can be applied in several areas of practice, but before the application of the method, it is an important step to validate the model and to understand the capabilities of the technique.

In the early model validation steps (the implementation of the energy source term and the Coriolis force was investigated), large-eddy simulations (LES) of small scale thermal convection problems were carried out in order to simulate urban heat island circulation problem (*Noto,* 1996; *Lu et al.,* 1997; *Cenedese* and *Monti,* 2003). Good qualitative and quantitative agreement was found regarding the velocity and temperature profiles and the general flow pattern as well. Behavior of a spreading density current has also been simulated by solving the unsteady Reynolds averaged Navier-Stokes (URANS) equations, to study the behavior of the dynamical model core and compare the differences between the incompressible and compressible versions of the model (*Kristóf et al.,* 2009). The correct implementation of the Coriolis force was also tested in this work.

These validation cases have the advantage of that they have more control over the measured parameters due to the nature of the measuring device. However, they have low Reynolds number range, the cases are mainly hydrostatic, the vertical extent is limited to a certain height, and the density current study used a fixed turbulence viscosity model.

The purpose of the present paper is to further extend the validation cases characterized by non-hydrostatic and strong nonlinear situations. Further differences compared to previous validations (*Kristóf et al.,* 2009) are the complex topography, the extended simulation domain height incorporating the tropopause, and that all the source terms are activated (see Eqs.(30)−(35)). Results of gravity wave simulations compared against the corresponding analytic solution, small scale water-tank experiments (*Gyüre* and *Jánosi,* 2003), and full scale observations (*Lilly* and *Zipser,* 1972) will be presented. The

simulation of such cases has been found to be ideal for testing and evaluating mesoscale numerical models due to the presence of complex flow patterns and wave breaking phenomena.

Atmospheric waves form when stable air flow passes over an obstacle. Fluid parcels tend to return into their original height due to the restoring forces caused by stratification. Various types of oscillatory flow responses occur depending on the state of stratification and geometric parameters (*Holton,* 2004). One can see two divisions of mountain waves, vertically propagating and trapped lee waves. Mountain waves vertically propagating over a barrier may have horizontal wavelengths of many tens of kilometers, even reaching the lower stratosphere (*Lin,* 2007). The vertical propagation of trapped lee waves is limited to a certain height due to the presence of a highly stable layer when waves can be reflected in such situations. In general, gravity waves can modify the local weather situation near mountains: they can create rotor motions, hydraulic jumps, and they have the capability of concentrating momentum on the lee slopes, or occasionally leading to violent downslope windstorms. (*Klemp* and *Lilly,* 1975; *Simon et al.,* 2006) Lee waves can be a potential hazard for wave gliders, by producing rotors or clear air turbulence. Flow beneath the wave crests can be extremely turbulent, thus causing a potential hazard for low-level aviation as well (National Research Council, 1983). The simulations of atmospheric scale flows around mountains can also have economical importance when the future location of a wind farm is to be estimated (*Montavon,* 1998; *Lopes da Costa et al.,* 2006; *Palma et al.,* 2008).

One can observe mountain waves (*Smith et al.,* 2002) with the help of various types of clouds, altocumulus or wave clouds at wave crests. Rotor clouds may dye some parts of the wave field if the appropriate amount of moisture is present. In some cases they are marked by regularly spaced clouds, and may be of great help to the flight of gliders (*Lesieur,* 2008).

Several researchers examined mountain waves and established theories to describe the basic phenomena (*Scorer,* 1949; *Long,* 1953; *Doyle and Durran,* 2002; *Smith,* 2002). One can also find experimental works dealing with the examination of flows around small scale, simplified, two-dimensional isolated obstacles (*Gyüre* and *Jánosi,* 2003). Gravity waves can be a good basis for the validation of atmospheric simulation models, as their structure strongly depends on the state of stratification. Indeed, one can see numerous works dealing with the validation of mesoscale models against mountain waves (*Durran* and *Klemp,* 1983; *Yang,* 1993; *Thunis* and *Clappier,* 2000; *Xue et al.,* 2000), such as the ones caused by a severe downslope windstorm event of Boulder. Similar events can occur in mountainous regions all over the world (*Colle and Mass,* 2000; *Belušič* and *Klai,* 2004). Postevent analysis of severe windstorms are often performed to study the future predictability of such events and also to test model performance and validity. A recent study dealt with the November 19, 2004 windstorm in the High Tatras in Slovakia (*Simon et al.,* 2006). The authors

concluded that an increased 2.5 km resolution mesoscale model can forecast downslope windstorms.

In the following section the main aspects of numerical models used in meteorological codes and in engineering CFD will be compared together with a brief description of the model transformations (for the full description see *Kristóf et al., 2009*). Simulation results will be shown in the third section in comparison with analytical solutions, water-tank experiments, and full scale downlsope windstorm observations. Conclusions and further investigations are outlined in Section 4.

2. Model overview

In this section a brief overview will be given on the governing equations, numerical methods, and parameterizations applied in numerical weather prediction (NWP) and CFD models in order to show the similarities and differences between the meteorological and engineering assumptions.

2.1. Meteorological outlook

The Navier-Stokes (N-S) equitation describes all types of fluid motion of our interest. It can be seen that today's NWP and CFD models are based on these equations of different forms.

2.1.1. Equations, numerical solution

Modern numerical forecast models are based on a formulation of the dynamical equations, which is essentially the formulation proposed by Richardson (*Lynch, 2006*):

$$\frac{d\mathbf{v}}{dt} = -2\mathbf{\Omega} \times \mathbf{v} - \frac{1}{\rho}\nabla p + \mathbf{g} + \mathbf{F_r} \ , \tag{1}$$

where $\mathbf{v}, \mathbf{\Omega}, \rho, p, \mathbf{g}$ *and* $\mathbf{F_r}$ are the velocity vector, angular velocity of the Earth, air density, pressure, gravity term, and the frictional force, respectively. The centrifugal force is combined with gravitation in the gravity term $\mathbf{g}$. This form of the N-S equation is basic to most work in dynamic meteorology and solved together with the continuity and thermodynamic equations and the equation of state in NWP-s. After expanding the components of Eq. (1), one arrives to the eastward, northward, and vertical components in spherical coordinate system, respectively (*Holton, 2004*):

$$\frac{du}{dt} - \frac{u\,v\,tan\,\varphi}{a} + \frac{u\,w}{a} = -\frac{1}{\rho}\frac{\partial p}{\partial x} + 2\Omega v\,sin\,\varphi - 2\Omega w\,cos\,\varphi + F_{rx}, \qquad (2)$$

$$\frac{dv}{dt} - \frac{u^{2}\,tan\,\varphi}{a} + \frac{v\,w}{a} = -\frac{1}{\rho}\frac{\partial p}{\partial y} - 2\Omega u\,sin\,\varphi + F_{ry}, \qquad (3)$$

$$\frac{dw}{dt} - \frac{u^{2}+v^{2}}{a} = -\frac{1}{\rho}\frac{\partial p}{\partial z} - g + 2\Omega u\,cos\,\varphi + F_{rz}, \qquad (4)$$

where u , v, w are the velocity components, a is the curvature of the Earth, φ is the latitude, and F_{ri} are the components of the frictional force. The terms standing with $1/a$ in Eqs. (2) – (4) are so-called curvature terms, and they arise due to the curvature of the Earth and often neglected in midlatitude synoptic scale motions.

The precise form of equations depends on the vertical coordinate system chosen as well, such as pressure coordinates, log pressure coordinates, sigma coordinates, hybrid coordinates, etc. (*Kasahara,* 1974; *Klemp et al.,* 2007; *Saito et al.,* 2007). Furthermore, the variables may be decomposed into mean and perturbation components. Equation systems using perturbation variables reduce the truncation errors in the horizontal pressure gradient calculations, in addition to reducing machine rounding errors in the vertical pressure gradient and buoyancy calculations. For this purpose, new variables are defined as perturbations from a hydrostatically-balanced reference state, and reference state variables are defined to satisfy the governing equations for an atmosphere at rest. (*Skamarock et al.,* 2005) As an example, in the hydrostatic model version of the Fifth-Generation Penn State/NCAR Mesoscale Model (MM5), the state variables are explicitly forecasted while in the non-hydrostatic model version (*Dudhia,* 1993) or in the more advanced Weather Research and Forecasting modeling system (WRF), pressure, temperature, and density are defined in terms of a reference state and perturbation components. When Reynolds averaging is applied, various covariance terms will appear in the system, representing turbulent fluxes. For many boundary layers, the magnitudes of the turbulent flux terms are of the same order as the other terms in Eqs. (2) – (4). In these cases one cannot neglect these fluxes even if it is not of direct interest.

There are tendencies towards higher spatial resolution models, but the resolution of most NWP models is yet too coarse to resolve boundary layer eddies, and parameterizations of them are usually necessary as the complete energy cascade cannot be resolved. (The High Resolution Limited Area models (HIRLAM), or ALADIN operate on horizontal grids in the range of 1–10 km.) Thus a number of turbulent mixing and filtering formulations were developed in the past. Some of these filters are for numerical reasons. For example,

divergence damping filters acoustic modes from the solution. Other filters represent sub-grid processes that cannot be resolved on the given spatial resolution.

2.1.2. Filtering of acoustic modes

The complete equations of motion (Eqs. (2) − (4)) describes all types and scales of atmospheric motion. The elimination of terms on scaling considerations has an important advantage of simplified mathematics and filtering of a range of unwanted type of motions.

These high-frequency acoustic modes would limit the time step during the calculation. To circumvent, different time discretization techniques are developed, see, e.g., the Runge-Kutta time-split scheme in *Wicker* and *Skamarock* (2002) or *Almut* and *Herzog* (2007). The efficiency of the time-split scheme arises from that the large time step Δt is much larger than the acoustic time step $\Delta \tau$, so the most costly calculations are only done in the less-frequent large steps. There are less efficient methods than the leapfrog-based models (e.g. in MM5 or WRF) resulting typically a factor of two greater time step. In the non-hydrostatic model of MM5, a semi-implicit scheme based on *Wilhelmson* and *Klemp* (1978) is used to filter the acoustic waves, while in the hydrostatic model, a split-explicit scheme based on *Madala* (1981) is used to filter gravity waves from the solution. The time differencing in MM5 is extensively discussed in *Grell et al.* (1995). In highly complicated systems, also involving pollution transport and chemical reactions, efficient operator splitting methods are developed recently to reduce computational time. The method is well spread in related fields of applied mathematics (*Geiser,* 2008) and in circulation and pollution models (*Havasi et al.,* 2001; *Faragó,* 2006; *Kocsis et. al,* 2009)

2.1.3. Planetary boundary layer (PBL) and surface-layer schemes, turbulence, closure problem

NWP and air pollution models must contain proper treatment for the PBL since it couples energy, momentum, and mass transfer between the land and atmosphere. The importance of its modeling is increasing nowadays due to environmental requirements, including human health, urban air quality, local and global warming trends, or homeland security problems. The PBL parameterization is especially important for predicting pollutant transport and dispersion (*Lundquist* and *Chan,* 2006).

In order to solve the equations of motion (Eqs. (2) − (4)), closure assumptions must be made to approximate the unknown fluxes as a function of known quantities and parameters (*Holton,* 2004). Turbulent fluxes provide a lower boundary condition for the vertical transport done in the PBL schemes. The PBL schemes determine the flux profiles within the well-mixed boundary layer and the surface layer providing tendencies of temperature, moisture, and

horizontal momentum in the entire column. Thus, when a PBL scheme is activated, explicit vertical diffusion is de-activated assuming that the PBL scheme will handle the process. Most PBL schemes apply dry mixing, but can also include moisture effects in the vertical stability that determines the mixing. The schemes are one-dimensional, since the horizontal large gradients cannot be resolved, and assume a clear scale separation between sub-grid eddies and resolved eddies. This assumption is less clear below a certain grid size, where boundary layer eddies may start to be resolved. In these situations the scheme is replaced by a fully three-dimensional local sub-grid turbulence scheme such as the turbulent kinetic energy (TKE) diffusion scheme (see in the WRF model: *Knievel et al.,* 2007; *Nagy,* 2010). Numerical simulations of PBL have been performed by many authors in the past resulting in different model complexity ranging from very simple zero dimensional parameterization to 3-D high resolution models. In the following sections a brief description will be given on the commonly used closure models.

2.1.3.1. First order closure

Operational NWP, emergency response, and air-quality models usually are of a RANS type (solving Reynolds averaged Navier-Stokes equations), and they employ first- or 1.5-order turbulence closures. The simplest turbulent transport parameterization is the first-order closure based on the K-theory (*Corrsin,* 1975; *Wyngaard* and *Brost,* 1984; *Holtslag* and *Moeng,* 1991; *Stull,* 1993). It is robust and requires low computational resources but gives poor approximation in the boundary layer, where the scale of typical turbulent eddies is strongly dependent on the distance to the surface and static stability. In many cases the most intense eddies have scales comparable to the boundary layer depth, and there the momentum and heat fluxes are not proportional to the local gradient of the mean. In much of the mixed layer, heat fluxes are positive even with neutral conditions.

To improve the model behavior, alternative approaches have been developed. An example is the modified first-order closure (*Townsend,* 1980; *Troen* and *Mahrt,* 1986; *Hong* and *Pan,* 1996). This scheme employs a counter-gradient flux for heat and moisture in unstable situations. It uses enhanced vertical flux coefficients in the PBL, and the PBL height is determined from a critical bulk Richardson number (Ri). It handles vertical diffusion with an implicit local scheme, and it is based on local Ri in the free atmosphere (Ri_{free}).

In spite of its drawbacks, the first-order closure based models remain the most popular parameterization for stable conditions, although alternative approaches have been used for the daytime convective period, e.g., the Blackadar (BK) non-local mixing scheme (*Blackadar,* 1976; *Zhang* and *Anthes,* 1982) and non-local K-theory (*Hong* and *Pan,* 1996). The BK scheme is a first-order hybrid local and nonlocal scheme in which eddy diffusivity, a function of

the local Ri number, is applied to the stable and forced convective regimes, while nonlocal mixing is used for free convective cases. The BK scheme's closure is based on an expression for the mass that is exchanged between individual layers in the boundary layer.

Recent improvements of first order schemes include the Yonsei University model (YSU, *Hong et al.,* 2006) or the asymmetrical convective models ACM1 (*Pleim* and *Chang,* 1992) and ACM2 (*Pleim,* 2007). YSU is based on the K profile for the convective cases as a function of local wind shear and local Ri_{free}. It also considers non-local mixing by adding a non-local gradient adjustment term to the vertical diffusion equation. Moreover, it contains additional terms to describe entrainment at the top of PBL proportional to the surface flux. For stable cases, the original mixing coefficient (*Hong et al.,* 2006) is replaced by an enhanced diffusion based on the bulk Ri number between the surface and top layers (*Hong,* 2010). The ACM1 and ACM2 models are modifications of the BK scheme. In ACM1 the symmetrical downward transport of BK scheme is replaced by an asymmetrical layer-by-layer model. In order to produce more realistic vertical profiles, the ACM2 model, a combination of local and non-local closures, was introduced (*Pleim,* 2007), that adds an eddy diffusion component to the non-local transport. With this addition the ACM2 scheme can better represent the shape of the vertical profiles in the near surface region. Both ACM1 and ACM2 models are available in the MM5 and WRF solvers.

2.1.3.2. Higher order closures

Given the known drawbacks of these simpler models, new approaches are developed with increasing complexity of turbulence description. The Gayno–Seaman (GS) scheme is a 1.5-order local closure scheme that computes eddy diffusivities based on local vertical wind shear, stability, turbulent kinetic energy (TKE) predicted by a prognostic equation (*Shafran et al.,* 2000), and length scale. The Eta PBL scheme, also known as the Mellor-Yamada-Janjic (MYJ) scheme (*Janjic,* 1990; *Mellor* and *Yamada,* 1982, *Janjic,* 1996, 2002), is a level-1.5 local closure scheme that computes vertical eddy diffusivities based on TKE predicted by a prognostic equation as a function of local vertical wind shear, stability, and turbulence length scale. The effects of the viscous sub-layer are taken into account through variable roughness length for temperature and humidity (*Zilitinkevich,* 1995). Other more sophisticated schemes are based on ensemble-averaged turbulence models (*Xue et al.,* 1996) with varying orders of closure (e.g., *Mellor* and *Yamada,* 1974; *Wyngaard et al.,* 1974; *Andre et al.,* 1978). These schemes often perform remarkably well under horizontally homogeneous conditions in modeling the horizontally (ensemble) averaged profiles of quasi-conservative quantities. However, the 3-D structures of the boundary layer is not predicted well. They are more complicated, and require solving equations of higher order moments, limiting their practical application

(*Lee et al.,* 2006). Several researcher proposed modifications to the original MY model improving the master length scale equation (*Sušelj and Sood,* 2010) or the pressure-strain, pressure –temperature covariance closures (*Nakanishi* and *Niino,* 2009)

Other researchers, however, showed that there is little gain in accuracy with increasing scheme complexity using different turbulence parameterizations. Increasing the complexity of the turbulence parameterization not just increased the computational resources but did not show obvious improvement, sometimes producing equally poor, if not worse, predictions (*Zhong et al.,* 2007) of the simulated mean and turbulent properties in the boundary layer, even around complex regions (*Berg et al.,* 2005).

Traditional PBL schemes were adequate for flat, horizontally homogeneous surfaces under steady-state conditions with different stratification. They cannot cope, however, with increased-resolution models that require more detailed and accurate representations of physical processes (*Baklanov et al.,* 2011). Therefore, different approaches are developed where the calculation of eddies was done explicitly in the PBL using 3-D high resolution models. Since only a small portion of the turbulence is handled by the subgrid scale (SGS) scheme, the results are less sensitive to turbulence closure assumptions. The first LES models and work in this area was pioneered by *Deardorff* (1974a,b). For PBL applications, LES models typically require horizontal resolutions on the order of 100 m (see, e.g., ARPS, MESO-NH codes), and they are typically used for research applications (e.g., *Weigel et al.,* 2007). *Deardorff* (1980) designed a simplified 1.5-order closure scheme that requires the solution of only one additional prognostic equation for the SGS turbulent kinetic energy, where the eddy coefficient was assumed to be proportional to the square root of TKE. This scheme has been widely used by researchers (*Klemp* and *Wilhelmson,* 1978) to handle SGS turbulence in cloud-scale models. Such models have a horizontal resolution in the order of 1 km, and they are expected to resolve cloud structures and limited turbulent eddies.

2.2. *Engineering outlook*

CFD tools have been in use for decades with success for solving engineering related problems involving broad range of physics. Spatial scales are extended to urban scales to handle flows involving pollution dispersion and can be even extended to mesoscale problems by the presented transformation method. Therefore, it is interesting to show the main aspects and some of the current problems of CFD solvers in this field.

2.2.1. *Governing equations, simulation of turbulent flows*

In engineering CFD, continuity, momentum, and energy equations are usually solved based on the finite volume method in an unsteady conservative form.

Because of numerous advantages of the finite volume method, it is widely spread among commercial and open source fluid mechanical solvers. Although the instantaneous Navier–Stokes equations exactly define all fluid flow, it is essentially impossible to solve these equations for turbulent flows over domains of significant spatial scale. Therefore, the exact equations are often Reynolds averaged to create a set of equations that can be solved for the spatial scales of engineering interest. The current adaptation method was developed for the commercial fluid mechanical solver ANSYS-FLUENT, but it can be implemented in other solvers as well, having user defined function (UDF) capabilities such as the commercial codes ANSYS-CFX and StarCD or the open source solver Openfoam. Through UDF-s, the user can modify the governing equations of the CFD code by adding appropriate source/sink terms to the equations.

The governing equations (Eqs. (5) – (7)) are solved by using the Boussinesq approximation (Eq. (10)) for the density.

$$\nabla \cdot \tilde{\mathbf{v}} = 0 , \tag{5}$$

$$\frac{\partial}{\partial t}\left(\rho_0 \tilde{\mathbf{v}}\right) + \nabla \cdot \left(\rho_0\, \tilde{\mathbf{v}} \otimes \tilde{\mathbf{v}}\right) = -\nabla \tilde{p} + \nabla \cdot \mathbf{\tau} + \left(\tilde{\rho} - \rho_0\right)\mathbf{g} + \mathbf{F} \tag{6}$$

$$\frac{\partial}{\partial t}\left(\rho_0 c_p \tilde{T}\right) + \nabla \cdot \left(\tilde{\mathbf{v}}\, \rho_0\, c_p \tilde{T}\right) = \nabla \cdot \left(K_t \nabla \tilde{T}\right) + S_T , \tag{7}$$

$$\frac{\partial}{\partial t}\left(\rho_0\, k\right) + \nabla \cdot \left(\rho_0\, \tilde{\mathbf{v}}\, k\right) = \nabla \cdot \left(\frac{\mu_t}{\sigma_k}\nabla k\right) + G_k + G_b - \rho_0\, \varepsilon + S_k , \tag{8}$$

$$\frac{\partial}{\partial t}\left(\rho_0\, \varepsilon\right) + \nabla \cdot \left(\rho_0\, \tilde{\mathbf{v}}\, \varepsilon\right) =$$

$$= \nabla \cdot \left(\frac{\mu_t}{\sigma_\varepsilon}\nabla \varepsilon\right) + \rho_0\, C_1\, S\, \varepsilon - \rho_0\, C_{2\varepsilon}\frac{\varepsilon^2}{k + \sqrt{v\,\varepsilon}} + C_{1\varepsilon}\frac{\varepsilon}{k}C_{3\varepsilon}G_b + S_\varepsilon , \tag{9}$$

$$\tilde{\rho} = \rho_0 - \rho_0\, \beta\left(\tilde{T} - T_0\right). \tag{10}$$

In the equation system $\tilde{\mathbf{v}}, \tilde{p}, \tilde{\rho}, \tilde{T}$ are the transformed field variables of velocity, pressure, density, and temperature. c_p and β are the specific heat capacity of dry air at constant pressure and the thermal expansion coefficient.

From the velocity vector ($\tilde{\mathbf{v}} = u\,\mathbf{i} + v\,\mathbf{j} + \tilde{w}\,\mathbf{k}$) only the vertical component was affected by the transformation. τ contains the viscous and turbulent stresses, $\mathbf{g} = -g\,\mathbf{k}$ is the gravitational force per unit mass, and $g = 9.81[\mathrm{N~kg}^{-1}]$. In the presented system the turbulent transport is modeled by the realizable k–ε turbulence model with full buoyancy effects (Eqs. (8) – (9)) developed by *Shih et al.* (1995). σ_k and σ_ε are the turbulent Prandtl numbers for k and ε, respectively. The turbulent viscosity μ_t and the turbulent heat conduction coefficient K_t are evaluated on the basis of turbulence kinetic energy (k) and dissipation rate (ε) fields (*Launder* and *Spalding,* 1972). The constant values of $C_{1\varepsilon}$, $C_{2\varepsilon}$, the expressions of C_1 and $C_{3\varepsilon}$, the turbulence production and buoyancy terms G_k and G_b, modulus of mean rate-of-strain tensor S can be referred either from CFD literature (*Shih et al.*, 1995) or from software documentation (*ANSYS Inc.,* 2012) of the applied simulation system. ρ_0 and T_0 are reference (sea level) values of density and temperature.

Volume sources S_T, S_k, and S_ε in Eqs. (7)–(9), as well as vector $\mathbf{F} = S_u\,\mathbf{i} + S_v\,\mathbf{j} + S_w\,\mathbf{k}$ in Eq. (6), are functions of local values of field (prognostic) variables, and used for adjusting the model to handle mesoscale effects. The components of the Coriolis force are included in $\mathbf{F}$ through S_u, S_v, and S_w.

Reynolds averaging introduces other unknowns into the equation system, the so-called Reynolds stresses. Since there is no existing general formula for the description of these stresses, large number of engineering turbulence models were developed applicable to certain flow features, but there are no turbulence models that would be generally applicable to all kind of turbulent flows. The modeling of these virtual stresses is still a major part of the today's turbulence modeling science. Different versions of two equation models are used in CFD for turbulence modeling. The most popular are versions of the k–ε model or other two equation models. These versions are denoted as linear eddy viscosity models, which adopt the Boussinesq approximation, implying an isotropic eddy viscosity. There were attempts using two equation models in NWP codes. An example is the implementation of a version of the k–ε model by *Hanjalic* and *Launder* (1972) in the MESO-NH meteorological code. It was not used extensively since, according to the authors, the current version did not give satisfactory results. The disadvantage of these eddy viscosity models is that they give an unrealistic representation of the normal turbulent stresses. This representation of the turbulent stresses produces fairly good results as long as only one of the turbulent stresses is dominant in the momentum equations. Further downside is that in more complicated flows, where more than one of the normal stresses is important, the ability of a turbulence model to predict normal stress anisotropy becomes significant. This motivates the development and application of nonlinear k–ε models (*Gatski* and *Jongen,* 2000) and other more advanced models, such as LES or hybrid RANS-LES models.

2.2.2. Stratification and turbulence models

One can find several works on the application of turbulence models in neutral conditions (*Richards and Hoxey,* 1993; *Blocken et al.,* 2007; *Hargreaves* and *Wright,* 2007). Stable stratification, however, causes drainage flows over uneven topography, intermittent turbulence, low-level jets, gravity waves, flow blocking, intrusions, and meandering, thus posing challenges in modeling of stable stratification (*Lee et al.,* 2006).

Several problems can be identified regarding the maintenance of turbulence profiles with distance (*Huser et al.,* 1997) dissipating turbulence early downstream of the obstacle (*Hanna et al.,* 2006). Treatment of these inconsistencies is the modification of the model constants of existing models (*Duynkerke,* 1988), adding source terms to the turbulent dissipation rate (TDR) equation for ε or a non-constant formulation for the $C_{1\varepsilon}$ parameter (*Freedman and Jacobson,* 2003; *Pontiggia et al.,* 2009). *Vendel et al.* (2010) proposed an inlet pressure profile and flux condition for the ground in order to define an appropriate downwind boundary condition for the stable or unstable cases.

Although CFD models are currently slow to be used for real-time emergency response, they can be used for planning purposes and to guide parameterizations of real-time wind flow models. A good example of a dispersion model that is parameterized based on the CFD results is the Quick Urban and Industrial Complex dispersion modeling system (*Williams et al.,* 2004). As computing power has become more affordable, CFD has become an increasingly valuable tool for studying urban flow. These models explicitly account for building geometry and require minimal parameterizations (*Balczó et al.,* 2011; *Balogh* and *Kristóf,* 2010). With the current model transformation, one can take into account mesoscale effects in the same numerical model with finely resolved topography.

2.2.3. System of transformations

The proper representation of Coriolis force, compressibility, and stratification effects is achieved by a system of transformations. These adjust the governing equations solved by the CFD solver through user defined volume source or sink terms. The CFD solver operates with transformed field variables (Eqs. (5)−(10)). Relations between untransformed physical quantities (T, p, ρ, z, w) and transformed ones ($\tilde{T}, \tilde{p}, \tilde{\rho}, \tilde{z}, \tilde{w}$) are defined by Eqs. (11)−(15).

$$T = \tilde{T} - T_0 + \overline{T}, \tag{11}$$

$$p = \frac{\overline{\rho}}{\rho_0}\, \tilde{p} + \overline{p} = Ce^{-\zeta\, z}\, \tilde{p} + \overline{p}, \tag{12}$$

$$\rho = \tilde{\rho} - \rho_0 + \bar{\rho}, \tag{13}$$

$$z = -\frac{1}{\zeta} \ln\left(e^{-\zeta z_{ref}} - \frac{\zeta}{C}\left(\tilde{z} - \tilde{z}_{ref}\right)\right), \tag{14}$$

$$w = \frac{\rho_0}{\bar{\rho}} \tilde{w} = \tilde{w} \, C^{-1} e^{\zeta z}, \tag{15}$$

where ζ is the density parameter described by Eq. (18) and z_{ref} is a reference altitude (Eq. (20)). Zero subscipt denotes values at ground level. The vertical extent of the atmosphere is "compressed" below a well-defined bound (C/ζ) described by Eq. (14), thus $\tilde{z} \to C/\zeta$, when $z \to \infty$, where C, described by Eq. (19), acts as a switch between the description of stratosphere and troposphere. The model utilizes an (x, y, z) Cartesian coordinate system. The Jacobian of the transformation of coordinate z can be calculated according to Eq. (16). $J \to 1$ when $\tilde{z} \to 0$, and therefore the geometrical transformation has a negligible effect close to ground.

$$J = \frac{dz}{d\tilde{z}} = C^{-1} \exp(\zeta \, z). \tag{16}$$

In this zone, the original form of the Cartesian equations existing in the CFD solver gives a good enough description for the flow close to the surface.

2.2.4. Reference profiles

The relationship between the absolute physical quantities and the field variables in the CFD solver are based on the reference profiles (distinguished by over-bars) Eqs. (21)−(29). It can be optimized to have the least possible deviation from the hydrostatic equilibrium and can simplify the specification of the initial conditions. These terms depend only on the vertical coordinate using approximation of the polytrophic atmosphere, as according to Eqs. (21)−(29). The original transformation expressions (*Kristóf et al.,* 2009) that were valid below an altitude of 11 km have been extended to incorporate the tropopause and the lower stratosphere up to an altitude of 25 km. For simplicity, the following double valued constants are introduced to describe these layers:

$$\gamma = \begin{cases} \gamma_t \ , \text{when } z < z_{tp} \\ 0 \ , \text{when } z \geq z_{tp} \end{cases}, \tag{17}$$

$$\zeta = \begin{cases} \zeta_t \ , \text{when } z < z_{tp} \\ \zeta_s \ , \text{when } z \geq z_{tp} \end{cases}, \tag{18}$$

$$C = \begin{cases} 1 \ , \qquad\qquad \text{when } z < z_{tp} \\ e^{(\zeta_s - \zeta_t)z_{tp}} \ , \quad \text{when } z \geq z_{tp} \end{cases}, \tag{19}$$

where subscripts t and s denote values for the troposphere and stratosphere, and z_{tp} is the tropopause altitude. In the stratospheric region we use z_{tp} as a reference altitude, therefore:

$$z_{ref} = \begin{cases} 0 \ , \text{when } z < z_{tp} \\ z_{tp} \ , \text{when } z \geq z_{tp} \end{cases}. \tag{20}$$

Using the above notations, the reference profiles for the troposphere will read as:

$$\overline{T_t} = T_0 - \gamma_t \ z, \tag{21}$$

$$\overline{p_t} = p_0 \left(\frac{T_0 - \gamma_t \ z}{T_0} \right)^{\frac{g}{R \ \gamma_t}}, \tag{22}$$

$$\overline{\rho_t} = \rho_0 \ e^{-\zeta_t \ z}, \tag{23}$$

$$\zeta_t = -\left(\frac{g - R\gamma_t}{z \ R \ \gamma_t} \right) \ln\left(1 - \frac{\gamma_t \ z}{T_0} \right). \tag{24}$$

The reference profiles in the stratospheric region are based on an isothermal temperature profile, therefore:

$$\overline{T_s} = T_{tp},\qquad(25)$$

$$\overline{p_s} = p_{tp}\,e^{-\zeta_s\left(z - z_{tp}\right)},\qquad(26)$$

$$\overline{\rho_s} = \rho_{tp}\,e^{-\zeta_s\left(z - z_{tp}\right)},\qquad(27)$$

$$\zeta_s = \frac{g}{RT_{tp}}.\qquad(28)$$

By using the above notations, the universal density profile reads:

$$\overline{\rho} = \rho_0 C\,e^{-\zeta\,z}.\qquad(29)$$

The constant values in Eqs. (21) – (29) can be optimized for a given case, but the standard ICAO (*Manual of the ICAO Standard Atmosphere,* Doc 7488, 1993) temperature and pressure profiles, based on the following constants, have been found to be suitable references for simple applications: $\gamma_t = 0.0065\ ^\circ\mathrm{C\ m^{-1}}$, $T_0 = 15\ ^\circ\mathrm{C}$, $p_0 = 1.01325 \cdot 10^5\ \mathrm{Pa}$, $\rho_0 = 1.225\ \mathrm{kg\ m^{-3}}$, $R = 287.05\ \mathrm{J\ kg^{-1}\ K^{-1}}$, $\zeta_t = 10^{-4}\cdot \mathrm{m^{-1}}$

2.2.5. Volume sources

The volume sources (Eqs. (30) – (35)) have been calculated according to Eqs. (20)–(25) by utilizing the UDF capability of the system.

$$S_u = \rho_0 fv - \rho_0 \ell\,\tilde{w}\,J,\qquad(30)$$

$$S_v = -\rho_0 fu,\qquad(31)$$

$$S_w = \rho_0\left(J^2 - 1\right)\left(\ell u\,J^{-1} + \beta\left(\tilde{T} - T_0\right)g\right) + \rho_0\,\ell u\,J^{-1} + \zeta\,J\left(\tilde{p} - \rho_0\tilde{w}^2\right),\qquad(32)$$

$$S_T = -\rho_0\,c_p\,\tilde{w}\left(\Gamma - \gamma\right)J,\qquad(33)$$

$$S_k = -\beta\,g\,\frac{\mu_t}{\mathrm{Pr}_t}\left(\Gamma - \gamma\right),\qquad(34)$$

$$S_\varepsilon = -C_{1\varepsilon} \; C_{3\varepsilon} \; \frac{\varepsilon}{k} \beta \; g \; \frac{\mu_t}{\Pr_t} \left(\Gamma - \gamma \right) . \tag{35}$$

In the above expressions, μ_t and $\Pr_t$ are the turbulent viscosity and turbulent Prandtl number, $f = 2\,\Omega \sin\varphi$ and $1 = 2\Omega \cos\varphi$ are the Coriolis parameters, φ is the average latitude, and Ω is the angular velocity of Earth. Moisture transport is not taken into account in the mathematical model, therefore the dry adiabatic temperature gradient Γ, appearing in Eqs. $(19) - (21)$, is calculated according to the assumption of a dry adiabatic process: $\Gamma = g/c_p = 0.00976 \; {}^\circ\text{C m}^{-1}$.

2.2.6. A simplified model version for water-tank experiments

Validation against small scale water tank experiments requires the adjustment of the transformation expressions. The working medium is liquid and the vertical extent of the device is small, therefore the atmospheric pressure variation with the vertical coordinate is negligible. Compressibility is not taken into account consequently ($\Gamma = 0, z = z$, and $\zeta_t = 0$). The vertical reference profiles for pressure and density are $\overline{\rho_t} = \rho_0, \overline{p_t} = p_0$. Due to the very weak turbulence characterizing these experiments, a laminar approach or LES method should be used instead of the k–ε model. The Coriolis force usually has a negligible effect in such experiments, and therefore, $\Omega = 0$ can be assumed.

These assumptions will simplify the source term acting on the energy equation:

$$S_{T,\,incomp} = \rho_0 \, c_p \, \widetilde{w} \, \gamma . \tag{36}$$

The values of $\gamma = - d\overline{T}/dz$, c_p, β, and T_0 for water-tank simulations can be calculated according to the temperature or density gradient of the fluid, maintaining the same Brunt-Väisälä frequency and material properties of the experiment.

2.2.7. Nesting

In NWP models the simplest method is the "one-way" downward nesting, where the outer model provides 4D boundary conditions to the inner higher resolution domain. In some cases it can be provided, if the mesoscale model horizontal resolution is as fine as a few hundred meters. The one-way nesting technique, in the Advanced Regional Prediction System (ARPS), allows adjustments in vertical resolution between grids, which is important for LES mode, where the

grid aspect ratio should be kept close to unity. In more advanced "two-way" nesting, the nested finer domain and the outer coarser domain interact at every time step of the outer coarse grid and, the microscale model provides lower boundary-condition to the outer domain. "With current computer capacities, this can be done within small parts of the mesoscale domain, which creates inconsistencies with the remaining parts of that domain." (*Baklanov et al.,* 2011) The current implementation of two-way nesting schemes in WRF or MM5 does not allow higher vertical resolution in the inner nesting levels, because the number of vertical levels must be the same for all levels (*Michioka* and *Chow,* 2008). Another problem that also exists in the CFD field is the velocity and length scale changes across the boundaries of nesting levels. This is especially important when the complex high resolution topography generates nonlinear motions close to these boundaries. One may also expect the damping of low frequency motions passing through the boundary and as a consequence providing an improper upstream turbulence field for the inner microscale model.

The advantage of the CFD approach is that it allows arbitrary mesh refinements in the simulation domain, resulting a continuous change of field variables around the finely resolved region. The possibility of nesting also exists in the CFD solver allowing different mesh resolution either horizontally or vertically on both sides of the domain interface, but one can avoid it with the existing mesh refinement options (*ANSYS Inc.,* 2012). In the following case studies, structured quad meshes can be used (without additional interfaces) due to the simplicity of the underlying geometries.

3. Results and discussion

The application of the model transformation will be presented in this section. Results will be compared against the analytical solution of linear, hydrostatic mountain wave field. Nonlinear and non-hydrostatic simulation cases are then compared to small scale water-tank experiments, and finally, a full scale nonlinear and non-hydrostatic downslope windstorm case will be shown against an inter-comparison study of NWP models and field measurements.

3.1. Verification with analytic solution

The simulations were compared with the analytic solution of a linear hydrostatic wave field. A Witch of Agnesi curve was used for the relief geometry,

$$z(x) = h \frac{a}{x^2 + a^2}, \tag{37}$$

where *h* and *a* are the obstacle height and half width, respectively. This geometry has been used extensively in the literature (*Wurtele et al.,* 1996), as an analytic solution can be derived for this shape. In order to obtain comparable results with water-tank experiments, the following material properties and working conditions were used:

$$\rho_0 = 998 \text{ kgm}^{-3},\ T_0 = 27\ ^{\circ}\text{C},\ \beta = 0.000207\ \text{K}^{-1},\ -\gamma = 832\ \text{K m}^{-1},\ \text{U} = 0.25\ \text{ms}^{-1}.$$

The Reynolds number, based on the inlet flow speed (*U*) and the obstacle height (*h*), was about 2500; therefore a laminar model was used. Compressibility and the Coriolis force were not taken into account. Free-slip wall and symmetry boundary conditions were applied at the lower and upper boundaries. A constant velocity and static pressure profile were prescribed as inlet and outlet conditions. The model was initialized with constant $\tilde{T} = T_0$, $\tilde{p} = p_0$, and uniform horizontal velocity $\tilde{U} = U_0$.

Based on the linear wave theory (Eq. (38)), an analytic solution can be found for hydrostatic problems with a constant Scorer parameter (*l*). The Scorer parameter is usually a function of the vertical coordinate, and it is derived from the wave equation for atmospheric gravity waves with an assumption of a two-dimensional, non-viscous, adiabatic flow (*Smith,* 1979; *Durran,* 1990). This parameter is most often used to forecast the existence of trapped lee waves, which can be expected when *l* decreases strongly with height. This is especially true if *l* decreases suddenly in the mid-troposphere due to the presence of a stable layer dividing the troposphere into a highly and a weekly stable layer. The square root of the parameter *l* (Eq. (40)) has units of wave number. The wave number of the lee wave (*l*) lies between l_{upper} of the upper layer and l_{lower} of the lower layer. Wide mountain ranges generate vertically propagating waves of wave numbers less than l_{upper}. Small obstacles, that force wave numbers greater than l_{lower}, produce waves that will vanish with height.

For hydrostatic problems, the development of the full analytic solution has been summarized by several researchers (*Alaka,* 1960; *Smith,* 1979). The combined governing equations were resulted in the deep Boussinesq equation (Eq. (38)) for *w*. The Scorer parameter *l* is defined by Eq. (38) and Eq. (39):

$$\frac{\partial^2 \left(\sqrt{\dfrac{\rho_0(z)}{\rho_0(z=0)}}\, w \right)}{\partial x^2} + \frac{\partial^2 \left(\sqrt{\dfrac{\rho_0(z)}{\rho_0(z=0)}}\, w \right)}{\partial z^2} - l^2(z) \left(\sqrt{\dfrac{\rho_0(z)}{\rho_0(z=0)}}\, w \right) = 0, \quad (38)$$

$$l^2(z) = \frac{N^2}{U^2} - \frac{1}{U}\frac{d^2 U}{dz^2} - \frac{1}{U}\frac{d\ln\rho}{dz}\frac{dU}{dz} - \frac{1}{4}\left(\frac{d\ln\rho}{dz}\right)^2 - \frac{1}{2}\left(\frac{d^2\ln\rho}{dz^2}\right), \quad (39)$$

where w is the perturbation vertical velocity, $N = \sqrt{-\dfrac{g}{\rho_0}\dfrac{\partial \rho(z)}{\partial z}}$ is the Brunt-Väisälä frequency, U is the inlet flow speed, ρ is the fluid density, and z is the vertical coordinate, respectively. For incompressible flow only the first two terms remain.

$$l^2(z) = \frac{N^2}{U^2} - \frac{1}{U}\frac{d^2 U}{dz^2}. \tag{40}$$

The first term on the right-hand side dominates in our case, and additionally, if a uniform velocity profile ($U = U_0$) and Brunt-Väisälä frequency (N) are used, Eq. (40) simplifies to:

$$l = \frac{N}{U}. \tag{41}$$

With the help of the Scorer formula, flows can be categorized on the basis of the following two dimensionless quantities:

$$F_x = a\,l, \quad F_z = h\,l. \tag{42}$$

When $F_x \gg 1$, the flow is essentially hydrostatic, while non-hydrostatic effects become important when $F_x \sim 1$ (*Schumann et al.*, 1987). Regarding the linearity, when $F_z \ll 1$, the flow is linear and nonlinear effects dominate, when the value approaches to $F_z \sim 1$. The borders are, however, not well-defined, and that is why one can find test cases marked as moderately hydrostatic or moderately nonlinear (*Thunis* and *Clappier,* 2000). Calculating these parameters using $a = 2$ m and $h = 0.01$ m, one can find that our setup is linear and hydrostatic with $l = 5.32\ \text{m}^{-1}$, $F_x = 10.64$, and $F_z = 0.0532$. In the case of hydrostatic flow, an analytic solution exists (Eq. (43)) for the vertical velocity field $w(x, z)$, based on Eq. (38):

$$w(x, z) = \sqrt{\frac{\rho_0(z = 0)}{\rho_0(z)}}\ U\, h\, a\ \frac{(x^2 - a^2)\sin(l \cdot z) - 2\,x\,a\,\cos(l \cdot z)}{(a^2 + x^2)^2}. \tag{43}$$

The vertical velocity contours have been plotted against the corresponding analytic solution on *Fig. 1*. The agreement between the two solutions is very good, with the magnitude of the vertical velocity in the numerical solution being only slightly smaller. The locations of velocity maxima, in the case of the CFD results, are shifted only moderately downward in the vertical direction.
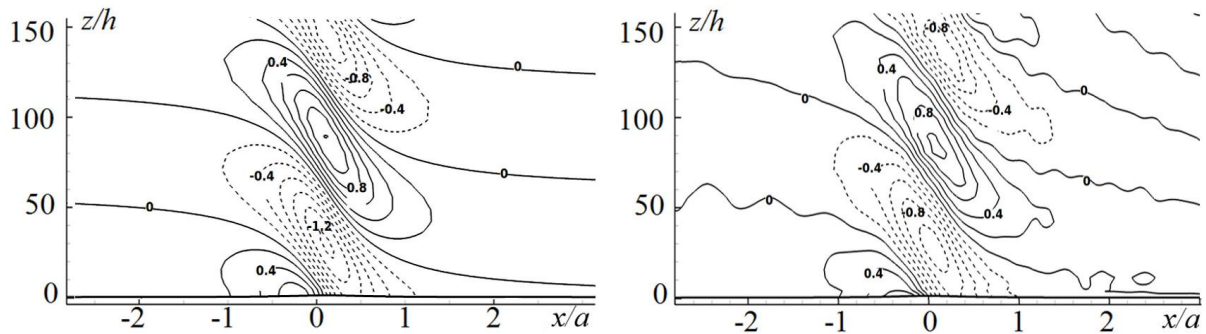
Fig. 1. Contour plots of the vertical velocity (w [mm s^{-1}]), obtained from the analytic solution based on Eq. (43) (left) and from CFD calculations (right). The solution is obtained for $U = 0.25$ m s^{-1}, $l = 5.32$ m^{-1}, $N = 1.3$ s^{-1}, $a = 2$ m, $h = 0.01$ m. The vertical and horizontal scales are normalized by the mountain height (h) and half width (a) respectively. Dashed lines represent negative values.

In the next section, a set of test cases have been prepared and the results are compared against experiments that cover a hydrostatic and nonlinear parameter range. The statistical performance measures applied for the comparison are also described briefly.

3.2. Statistical performance measures used during the evaluation

To quantitatively evaluate the output of the model with observations, *Hanna et al.* (1991, 1993) recommend the use of the following statistical performance measures (*Chang et al.,* 2005): the fractional bias (FB), the normalized mean-square error (NMSE), the fraction of predictions within a factor of 2 of observations (FAC2), and the hit rate (HR). *Chang* and *Hanna* (2004) suggest that a good model would be expected to have about 50% of the predictions within a factor of 2 of the observations (i.e., FAC2 > 0.5), a relative mean bias within 30% of the mean (i.e., –0.3 < FB < 0.3), a relative scatter of about a factor of 2 or 3 of the mean (i.e., NMSE < 4), and a hit rate above 66% (HR > 0.66) with an allowed deviation of D = 0.25. The absolute value of the model's fractional bias (FB) is reasonably good if it is less than 0.25. A tendency toward overprediction of wind speeds is seen, with the fractional bias regularly between 0 and –0.25 (*Lundquist* and *Chan,* 2006). The perfect model would have the following idealized performances: FAC2 = HR = 1 and FB = NMSE = 0. In air quality modeling, typical values of the above statistical

measures have been defined as acceptable for model evaluation and also correspond to a model acceptance criterion (*Chang* and *Hanna,* 2004).

3.3. *Numerical model results compared to small scale water-tank experiments*

Among the experiments focused on topography-induced gravity waves, one can find investigations dealing with symmetric and asymmetric obstacles, looking at the effect of asymmetry (*Gyüre* and *Jánosi,* 2003), determining surface drag by numerical simulations (*Klemp* and *Lilly,* 1975) and numerically examining the wave breaking characteristics (*Doyle et al.,* 2000; *Afanasyev* and *Peltier,* 2001). The common feature of the former experiments is the experimental apparatus. They use mainly the water as working medium, since in water it is relatively easy to generate and maintain stable stratification for a longer period of time. Usually, this is done by using layered salt water. The achievable range of Reynolds number is limited to approximately 10^3. In spite of this fact, these methods are widely used, since there is more control on the parameters and conditions, than in real atmosphere.

Two-dimensional simulations of internal gravity waves have been carried out by using symmetric and asymmetric obstacles, in correspondence with the experiments performed by *Gyüre* and *Jánosi* (2003). Obstacle shapes have been characterized by the following function:

$$z(x) = a \exp\left(-b / x / 2k\right), \tag{44}$$

where *a, b,* and *k* are shape parameters and *x* is the horizontal coordinate of the obstacle. Both the symmetric and asymmetric shapes can be described by Eq. (44), by prescribing different parameters for the upstream and downstream part of the mountain barrier. Measurements were performed in a narrow plexi glass tank of $2.4 \text{ m} \times 0.087 \text{ m} \times 0.4 \text{ m}$ filled with linearly stratified salt water, by towing the obstacles along the bottom of the tank at a constant speed. The range of the experimental parameters (obstacle height $h = 0.02 - 0.04$ m, towing velocity $U = 0.01 - 0.15 \text{ m s}^{-1}$, and Brunt-Väisälä frequency $N = 1.09 - 1.55 \text{ s}^{-1}$) corresponds to an atmospheric flow up to an elevation of $5 - 10$ km for an obstacle height of 600 m and a wind speed of $10 - 70 \text{ m s}^{-1}$ for a large range of hydrostatic state and linearity.

The flow was considered unsteady, incompressible, and two-dimensional in the simulation. Due to the low Reynolds number range, a laminar model was used. The domain was discretized with a structured quad grid, using 150 x 800 quad elements (*Fig. 2*). Second order time discretization, pressure staggering option (PRESTO) for pressure interpolation (*ANSYS Inc.,* 2012), and second order upwinding methods were used when solving the momentum and energy equations. Compressibility was turned off in this case by using the transformation described in Section 2.2.6.
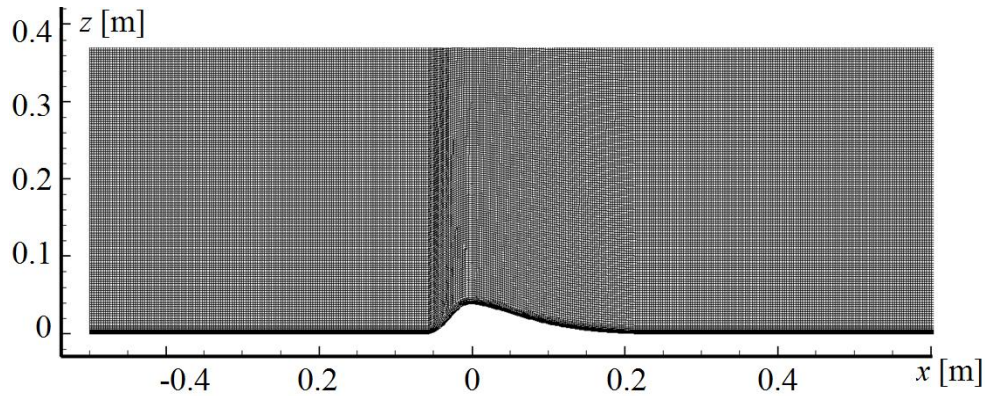
Fig. 2. Computational domain and numerical grid in the case of a gentle leeward side obstacle.

Typically for higher flow velocities, we observed flow separation during the simulation of symmetric steep lee-side obstacles. The separation induced bubble modified the shape of the leeward side in this case, quasi elongating the obstacle (*Fig. 3*), consequently changing the hydrodynamic characteristics of the barrier. Therefore, these cases were excluded from the comparison.
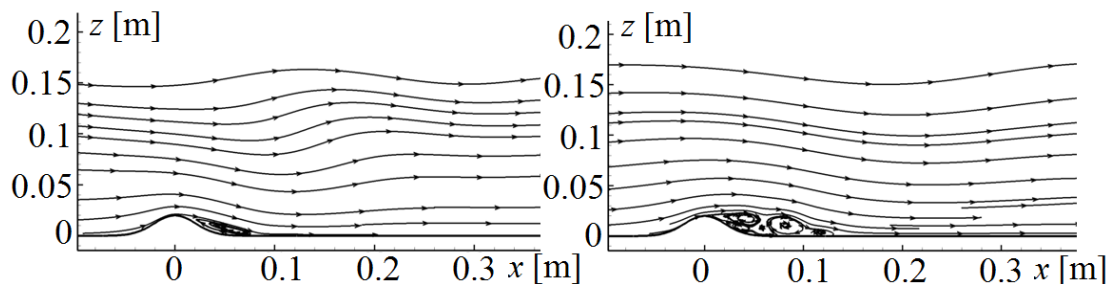

Fig. 3. Computed streamlines of the velocity field for *U/Nh* = 0.7 (left) and *U/Nh* = 1 (right) showing the elongation of the separation bubble and of the wave lengths for a symmetric obstacle.

In the numerical model, flow enters into the domain with a uniform inlet velocity profile. A moving bottom wall, for simulating the stationary bottom wall of the experiment was used. No visible disturbances were observed on the water surface, consequently a rigid lid (symmetry) with free slip boundary condition was applied in the simulation model. Avoiding the interaction between upward propagating and reflected wave fronts, data extraction was made after a short transient period, before interference could occur. This period was estimated from the vertical group velocity (*Gyüre* and *Jánosi,* 2003), which was proportional to the towing speed. In those cases where steepening and wave breaking occurred, samples were excluded from the averaging of amplitudes and wavelengths.

In *Table 1*, the simulations were categorized into four groups based on $F_x = Na/U$ and $F_z = Nh/U$ non-dimensional numbers as described by Eq. (42). These groups are nonlinear (NL), moderately nonlinear (M–NL), hydrostatic (H), and moderately non-hydrostatic (M–NH) cases. For all cases, the mountain height h, was 0.04 m, the leeward half width a, was 0.13 m, the Brunt-Väisälä frequency N, was 1.33 s^{-1} and U was the incoming flow velocity corresponding to the towing velocities of the obstacle in the survey.

Table 1. List of cases and parameters for the simulation of the gentle leeward side obstacle. Vertical structure and linearity categories are: H – hydrostatic, M-NH – moderately non-hydrostatic, NL – nonlinear, M–NL – moderately nonlinear

Case No.	U (m s^{-1})	Na/U	Nh/U	Vertical structure	Linearity
1	0.016	10.80	3.33	H	NL
2	0.032	5.31	1.64		
3	0.037	4.63	1.43		
4	0.041	4.15	1.28		
5	0.048	3.60	1.11		
6	0.053	3.24	1.00		
7	0.077	2.23	0.69	M–NH	M–NL
8	0.106	1.62	0.50		
9	0.160	1.08	0.33		

Wavelengths and amplitudes were measured in multiple positions above and downstream of the obstacle, by locating the wave fronts and measuring the distance between the fronts. The error bars in *Fig. 4* show the standard deviation of both the measured and simulated values. Circular wave fronts assumed in the case when lee waves are generated by a moving point source (*Voisin,* 1994). As shown from the upper part of *Fig. 5*, the shape of the wave fronts has been strongly affected by the obstacle shape, even in the M–NL cases. Here the centers of the wave fronts were gradually shifted toward negative coordinates, indicating strong wave dispersion. The large error bars of the measurements (*Fig. 4*) represent not only the limited resolution caused by the visualization technique (dying of different layers), but are also the consequence of the aforementioned strong dispersion of lee waves.

It was observed that our model performs well in the H–NL range for steeper lee-side obstacles, like the one presented in *Fig. 3*. However, close to the M–NH range with the same obstacle, results tend to differ from the experiments. This difference may be explained by boundary layer separation effects. At an increased velocity, the separation bubble that developed behind the obstacle elongated and caused the virtual mountain half width (mountain half width plus the horizontal size of the separation) and consequently the normalized wave length to almost double. (See the wave field in *Fig. 3*)
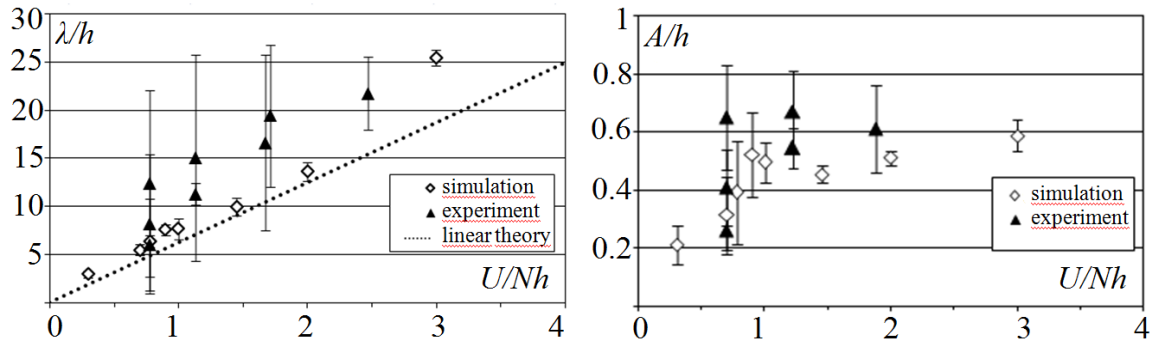
Fig. 4. Normalized averaged wave length (λ/h) (left) and normalized averaged wave amplitude (A/h) (right) as a function of non-dimensional horizontal flow velocity, in the case of the gentle leeward slope. The dotted line represents the wave length obtained from a linear theory, based on $\lambda = 2\pi U / N$ (*Scorer,* 1949). Filled symbols represent the measurements of *Gyüre* and *Jánosi* (2003). Error bars indicate the error originating from the data extraction technicque and wave dispersion.
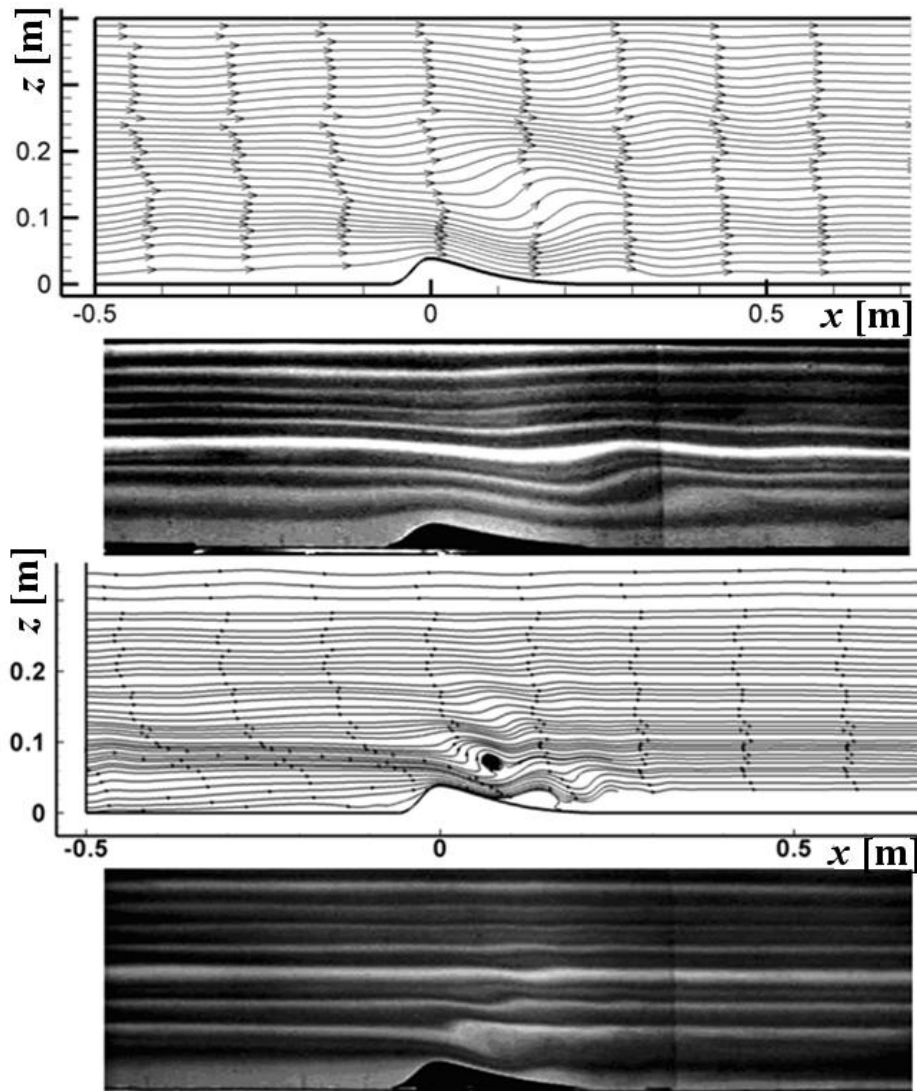

Fig. 5. Contours of computed streamlines and wave fields from the experiments (courtesy of *Gyüre* and *Jánosi,* 2003) at *Nh/U* = 0.69 (the upper two) and *Nh/U* = 3.33 (the lower two) non-dimensional flow velocities.

According to experimentalists (*Qiu* and *Xia,* 1998; *Gyüre* and *Jánosi,* 2003), the side walls have a negligible overall effect on the experimental results, however, the exact location and size of the separation were not captured properly, which can possibly be explained by the 3-D structure of the flow characterizing the laboratory experiments, due to the boundary layer on the side walls interacting with the separation bubble. In the case of a 3-D narrow obstacle, the separation bubbles were smaller, as the stratified flow tended to flow around the obstacle, instead of flowing over it. The prediction of the location of separation is currently a difficult topic, it requires the modeling of transitional turbulence and is beyond the scope of this investigation. Avoiding separation by using a gentle leeward side obstacle, however, gave both qualitative and quantitative agreements concerning the normalized amplitudes and wavelengths (*Fig. 4*). *Table 2* shows the performance measures, indicating good model performance. At low inlet velocities (bottom of *Fig. 5*), where wave breaking and rotors occurred, the flow structures, characterized by a high nonlinearity, were also captured properly.

Table 2. Statistic metrics of normalized wavelength *(λ/h)* and amplitude *(A/h)* for water-tank studies using CFD and experimental data of *Gyüre and Jánosi* (2003). Definition and the applied limits for the statistic metrics are described in *Chang et al.* (2005)

Validation metric	Abbreviation	Limit	λ/h	A/h	Classification
Correlation coefficient	R	>0.8	0.95	0.99	good
Fractional bias	FB	±0.3	0.317	0.21	good
Normalized mean square error	NMSE	0–4	0.12	0.05	good
Hit rate	HR	>0.66	0.75	1	good
Fraction of predictions within a factor of two of observations	FAC2	>0.5	1	1	good

3.4. Model comparison with a full scale event

3.4.1. Case study

A relatively well documented and studied event occurred during the winter of 1972 near Boulder, Colorado, where a severe wind storm, with a strong descent of air originating from the higher atmosphere, caused significant damage to the environment (*Lilly* and *Zipser,* 1972; *Brinkman,* 1974). The strong tropospheric descent is well reflected in the potential temperature contours in *Fig. 6a*, where the contours become denser close to the ground. The accompanying near ground downwind was also reported as being especially severe. A hydraulic jump and waves also developed behind the mountain (*Fig. 6a*).
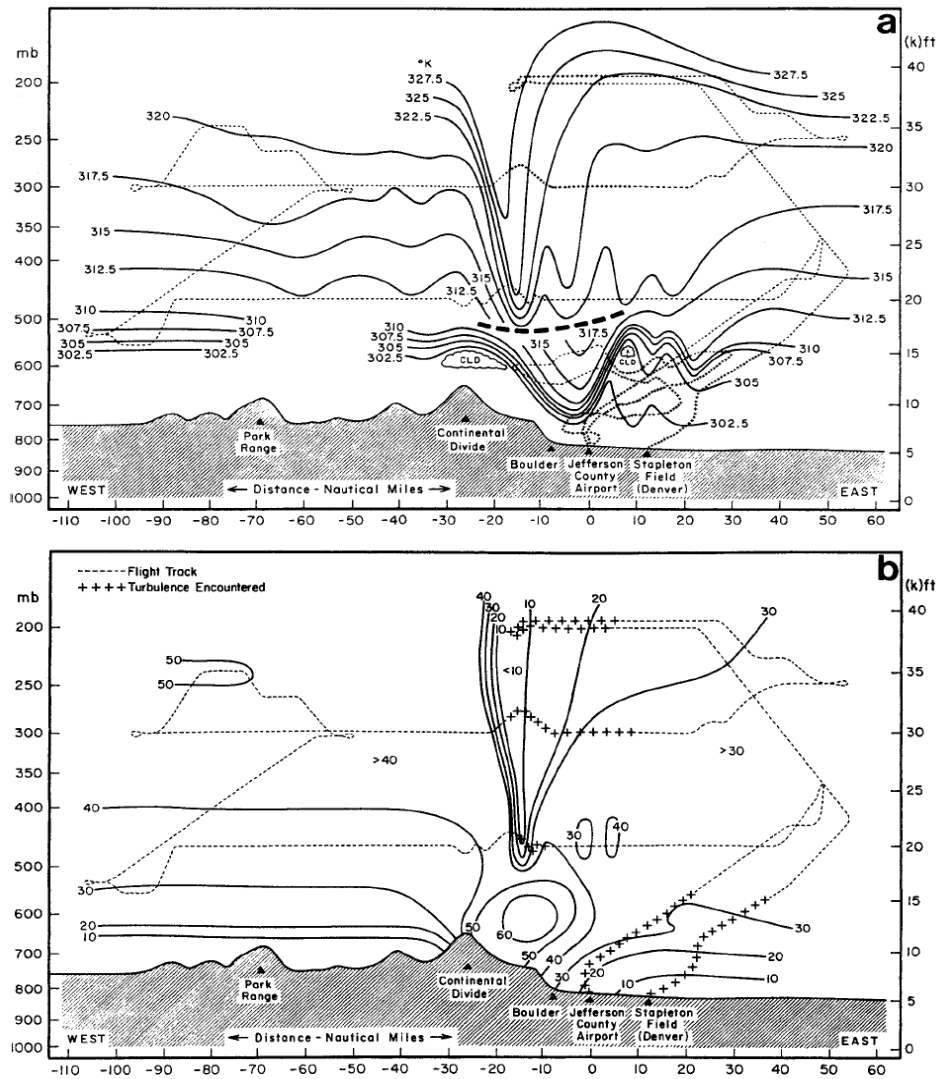
Fig. 6. Analysis of the potential temperature (a) and the horizontal velocity component (b) from aircraft flight data and sondes taken on January 11, 1972. Aircraft tracks are shown by dashed lines with the locations of significant turbulence indicated by plus signs (*Klemp* and *Lilly,* 1975).

The purpose of the present simulation is to show that the model is able to capture the main features and nonlinearities of such flows, for example the existence of the mentioned nonlinearities. This event became a standard test case of researchers (see ,e.g., *Xue et al.,* 2000) for developing simulation models, or to reproduce and understand the related mechanisms of such phenomena. A recent study dealt with the development of a severe thunderstorm in Budapest. With high resolution numerical modeling using MM5, they were able to reproduce the main features of the severe convective storm (*Horváth et al.,* 2007).

Different assumptions are made during similar case studies, in order to reduce computational cost, taking the advantage of the quasi two-dimensionality of the flow, or simply investigating each flow phenomena separately. Although mountain flows are generally three-dimensional, two-dimensionality can be a

good assumption for the downslope windstorm case, as the continental divide is long compared to its cross section. This is acceptable only if the large scale flow is being investigated and the microstructure has only negligible influence on the main flow. In some cases these structures have an effect, e.g., by modifying the horizontal position of the hydraulic jump. This is due to the increased surface friction resulting from a non-slip boundary. In spite these differences in the treatment of the lower boundary, the main features of the flow will still remain.

The elevation of the realistic terrain of the E–W oriented section was derived from a 3 arc second resolution SRTM (Shuttle Radar Topographic Mission) database. The section was then interpolated for the latitude of 40.015 N. The longitudinal coordinates were between 107.100 W and 103.900 W, giving an approximately 270 km wide section. The new coordinates were transformed onto the Universal Transverse Mercator (UTM) coordinates and were interpolated onto an approximately 1.5 arc second grid using a bicubic spline method.

Test cases using an idealized geometry have also been examined, where a simplified two-dimensional model has been used. In spite of the fact, that the real mountain has a plateau-like shape, due to the upstream influence and partial blocking, the upstream mountain profile does not affect significantly the upstream flow. Due to this fact, a symmetric mountain profile was used in several works (*Klemp* and *Lilly,* 1975), as well as in this study. The profile described by Eq. (37) was used for modeling both the upstream and downstream sections of the geometry. Here $a = 10$ km and $h = 2$ km are the mountain half width and height, respectively. The initial temperature and velocity profiles were based on the intercomparison study of *Doyle et al.* (2000). They found that these initial conditions were more appropriate for wave breaking tests, and more realistic than the conditions used in earlier studies (*Peltier* and *Clark,* 1979). Conditions favorable for downslope windstorms are usually characterized by strong cross mountain winds, and by the presence of a stable layer at the appropriate height (*Durran,* 1986). Both of these conditions were present in the studied situation.

The solution was found to be sensitive to the grid resolution (*Doyle et al.* 2000), therefore, in this study a relatively higher resolution grid was used. An equidistant grid was applied with a size of 1000 m and adapted to 250 m in two steps in the vicinity of the mountain. In the vertical direction the mesh size decreased down to 10 m resolution close to the ground. The domain extended from 2 to 25 km in the vertical and – 115 to 120 km in the horizontal direction, with the mountain crest positioned at $x = 0$ km. The top boundary was defined as symmetry with zero normal velocity, and the bottom was defined as a free-slip wall. A standard non-reflective boundary condition (outflow) was applied as an outlet. This means that the internal pressure field has been extrapolated to the outlet surface, and therefore, no further information on the outlet velocity and pressure profiles were required by the system.

Second order time discretization, pressure staggering option (PRESTO) for pressure interpolation (*ANSYS Inc.*, 2012), and second order upwinding methods were used in the momentum and energy equations. Compressibility was introduced with the help of the transformation used for model adaption. Moist effect and the Coriolis force were not considered during the calculations.

By using the ANSYS–FLUENT 13 simulation system, the model was integrated for a non-dimensional period of time of $t^* = \overline{U}t/a = 43.2$, based on an average inlet flow speed of 30 $\mathrm{m\,s^{-1}}$, which corresponds to a 4-hour flow time. The results shown in this section are obtained at $t^* = 32.4$ time instant. Results were quantitatively compared to several mesoscale meteorological codes using statistical performance measures described in Section 3.2. The summary of the comparison can be seen in *Table 3*. Based on FB, NMSE, and FAC2, the idealized model can be considered acceptable. Negative FB values indicate lower predicted overall horizontal velocity. The correlation coefficient and hit rate, however, show values under the limit. The hit rate was calculated with 5 $\mathrm{m\,s^{-1}}$ absolute and 10% relative deviation for the velocity and 1 K and 5% for the temperature, respectively, since large deviations with a factor of 2 differences were realized among the different intercomparision cases presented by *Doyle et al.* (2000). *Chang* and *Hanna* (2004) suggest that the model performance should not be judged based only on the performance measures but together with the comparison of flow patterns or the time evolution of the flow field.

Table 3. Statistic metrics calculated for horizontal velocity (*U*) and potential temperature (*Θ*) for the Boulder windstorm case study comparing CFD and NWP (*Doyle et al.,* 2000) model results

Validation metric	Abbreviation	Limit	*U*	*Θ*	Classification
Correlation coefficient	R	>0.8	0.154	0.96	not sufficient
Fractional bias	FB	±0.3	–0.07	–0.056	good
Normalized mean square error	NMSE	0–4	0.396	0.01	good
Hit rate	HR	>0.66	0.29	0.56	not sufficient
Fraction of predictions within a factor of two of observations	FAC2	>0.5	0.7	1	good

According to the experiments of *Doyle et al.* (2000), the results were highly time dependent, and therefore, unsteady simulations were executed and time-averaging was applied on the results. An averaging interval varying from 10 to 60 minutes was applied during the simulation, and it was found that the value and location of the maximum velocity were not affected. The horizontal position of the upstream edge of the hydraulic jump however changed significantly. The lee-slope wind magnitude varied considerably among the model simulations

presented by *Doyle et al.* (2000), and these differences were also reflected in the horizontal position of the hydraulic jump. The location of the upstream edge in some models, e.g., the *Durran* and *Klemp* (1983) model (DK83) or the Eulerian/semi-Lagrangian model (EULAG) was positioned immediately after the lee slope, similarly to our results, while in other cases it was positioned $10-25$ km downstream of that (e.g., MESONH, RAMS, or RIMS models of the same intercomparison). This partially explains the lower HR and R values due to the horizontal shift in the flow pattern. Regarding the downslope wind, a higher value of maximum horizontal velocity was realized by the simulation than that of the onsite measurements. At $t^* = 32.4$, the location of the maximum velocity peak was found at approximately 8.5 km downstream of the mountain crest at a height of 7 km (*Fig. 7*). With further integration, the locations of the maxima were shifted downstream to approximately 16 km beyond the crest and to a lower height of 4 km (bottom of *Fig. 7*). The magnitudes were not changed considerably, stabilizing at around 66 m s^{-1}. Regarding the wind speed close to the ground, within the lowest 50 m, $51-59$ m s^{-1} was realized, depending on the position along the mountain lee side. The near ground values of velocity magnitude were in fair agreement both with the observations and the meteorological models. The high instantaneous velocity peaks at higher altitudes obtained from the simulation could be partly caused by the lack of moisture transport and phase change processes. According to *Durran* and *Klemp* (1983), the wave response could be even 50% lower if a proper treatment for moist air flow is applied. This could significantly affect the properties of wave breaking, and consequently the development of a low level jet.

Several mesoscale codes simulated multiple breaking regions with the strongest ones located above the hydraulic jump at an altitude of 12 km and above (see the model results of RAMS, MESONH models presented by *Doyle et al.* (2000)). Wave steepening regions were obtained by CFD for the ideal and real mountain profiles at a similar altitude (between 10 and 15 km). Using the idealized geometry (*Fig. 7*), this region was weaker. The altitude of the maximum steepness above the hydraulic jump in the breaking region was at about 12 km with the highest amplitude waves being of 2–2.5 km.

The present results show smooth downstream isolines. In some of the cases of *Doyle et al.* (2000), the downstream part of the hydraulic jump was oscillatory, while in other cases the isolines were smooth. Among the results of different mesoscale meteorological solvers, depending on the amount of applied eddy diffusivity (K_d), different flow structures were obtained. Smaller K_d values usually resulted in smaller wave structures.

The stratospheric air descent reached the altitude of 5–6 km using the real topography which correlates well with the non-hydrostatic mesoscale vorticity (TVM) model solution of *Thunis* and *Clappier* (2000), or the model comparisons presented by *Doyle et al.* (2000) (CUMM, RAMS, RIMS). The descent was even stronger and propagated to lower altitudes in the case of the

simplified geometry accompanied by high TKE values (see *Fig. 7*) . The highest peaks, even reaching 117 $m^2 s^{-2}$, can be found around the upstream edge of the hydraulic jump and at the wave steepening regions at higher altitudes. The maximum value of TKE is reported approximately 15–20 $m^2 s^{-2}$ in atmospheric rotors (*Doyle et al.,* 2002) and even reaches higher values in the case of extremely severe turbulence.
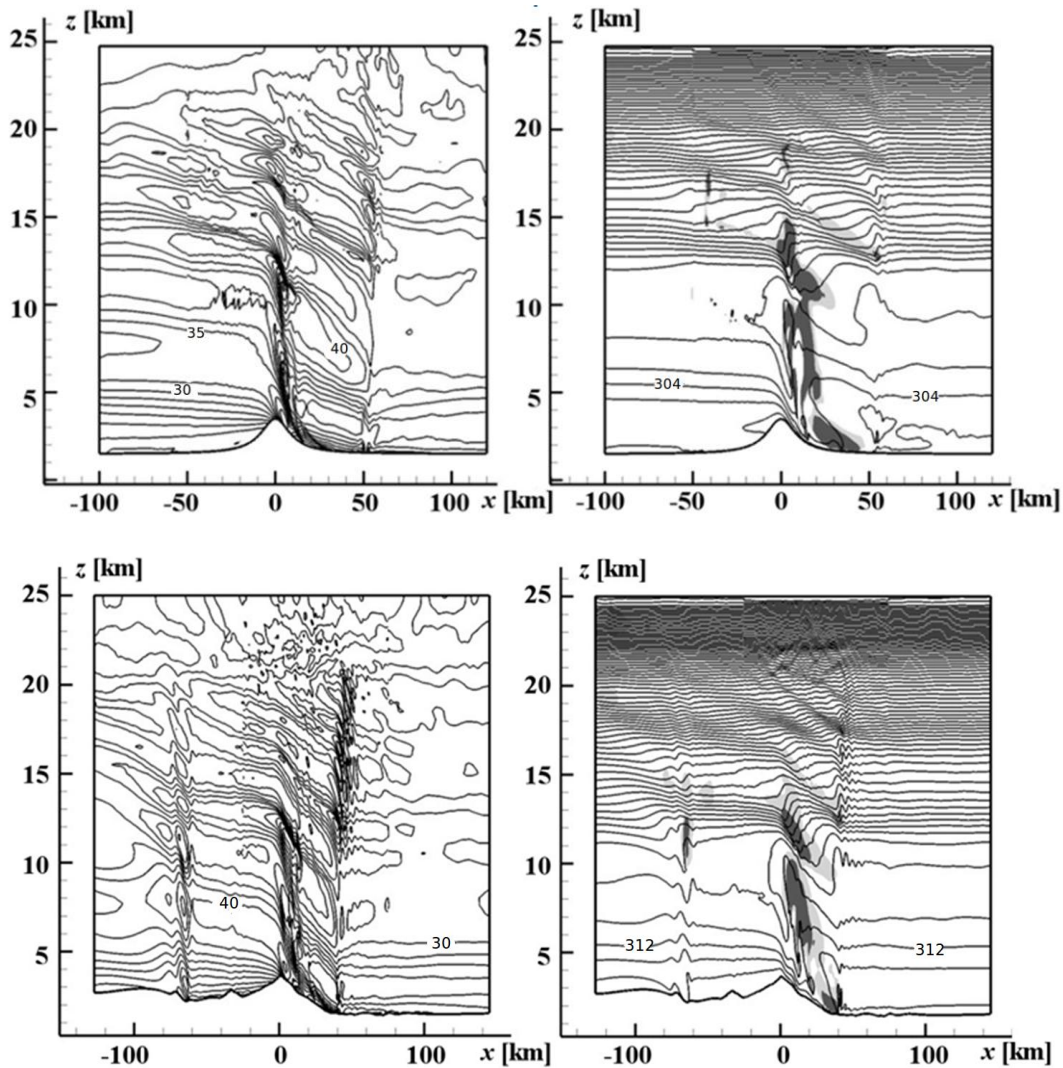
Fig. 7. Contours of horizontal velocity component (left panel) and potential temperature (right panel) for an idealized (top) and a real (bottom) mountain shape. The pictures show the results at $t^* = 32.4$ non-dimensional flow time. Vertical coordinates were magnified by a factor of 12 for better visualization. Potential temperature and velocity contour intervals are 8°C and 5 m s^{-1}, respectively. Light and dark grey areas indicate regions characterized by turbulent kinetic energy higher than 5 $m^2 s^{-2}$ and between 5–25 $m^2 s^{-2}$.

Differences in the magnitude of the horizontal velocity may also be related to the two-dimensional treatment of the topography if compared to the real situation. In three spatial dimensions, the flow can pass around the obstacle,

while in 2-D it is forced over it. The test results of *Doyle et al.* (2000) confirmed that a significant reduction in wave breaking could be found for the 3-D case. Some of the studies dealing with gravity wave evolution used a frictionless lower boundary (*Richard et al.,* 1989). Concerning the bottom boundary condition, a more realistic treatment of the ground surface could result in a slower movement and different horizontal location of the hydraulic jump.

4. *Summary and conclusions*

We briefly presented an adaptation method applicable to general purpose CFD solvers for atmospheric flow simulations, which was based on the application of an incompressible fluid model. Mesoscale effects, such as thermal stratification, adiabatic cooling caused by hydrostatic pressure driven expansion, compressibility, and Coriolis force were taken into account with the help of a transformation system and customized volume sources.

In this paper, simulations were presented around more complex geometrical features, idealized barriers, and real terrain, demonstrating the capabilities of the CFD based approach.

Simulations of linear hydrostatic waves were compared to an analytical solution, and it was stated that for this regime the code behaved well, and an excellent agreement was found.

Secondly, the simulation results were compared to water-tank experiments of two-dimensional mountain waves with different degrees of nonlinearity and hydrostacity. A good agreement was found based on the statistical performance measures and flow pattern comparison concerning the measured and simulated wavelengths and amplitudes. The model evaluation for λ/h gave a correlation coefficient of 0.95, fractional bias 0.317, normalized mean square error of 0.12, a hitrate value of 0.75 and 100% of predictions within a factor of two of observations. The equivalent results for A/h were 0.99 (R), 0.21 (FB), 0.05 (NMSE), 1 (HR), and 100% (FAC2). The model was also able to capture well the location and size of the appearing nonlinear structures, such as the rotor that was formed behind the obstacle.

Simulation of the Boulder windstorm case is ideal for testing and evaluating mesoscale numerical models, therefore it was chosen as the third object of analysis. The simulation results were compared to the on-site observations and a series of modeling experiments that were presented by *Doyle et al.* (2000). Model evaluation has demonstrated reasonable agreement with measurements for potential temperature (Θ). The model evaluation statistics gave a correlation coefficient of 0.96 and fractional bias –0.056, normalized mean square error of 0.01, a hit rate value of 0.56, and 100% of predictions within a factor of two of observations. The equivalent results for horizontal velocity (U) were 0.154 (R), –0.07 (FB), 0.396 (NMSE), 0.29 (HR) and

0.7 (FAC2). Results obtained from our simulations are encouraging with regard to the predictability of a low level, highly accelerated channel flow, and upper level wave breaking. Close to the ground a very strong lee-side wind was realized, accompanied by a well-defined hydraulic jump downstream.

Using only one single unstructured grid and a uniform physical description for close- and far-field flow, one can take the advantage of the model adaption in the simulation of mesoscale atmospheric phenomena. In the same model, one can investigate the finely structured microscale flow around complex geometrical features, such as flow around buildings with pollution dispersion or to study the close- and far-field of cooling towers and its effects to the environment.

The implementation and evaluation of non-reflective boundaries is planned through a 3-D mountain wave and associated downslope windstorm case study and the inclusion of moisture transport and phase change processes is also an important further step towards the practical application of the method.

References

Afanasyev, Y.D. and *Peltier, W.R.,* 2001: Numerical simulations of internal gravity wave breaking in the middle atmosphere: the influence of dispersion and three-dimensionalization. *J. Atmos. Sci. 58*, 132–153.

Alaka, M.A., Ed., 1960: The airflow over mountains. *WMO Tech. Note* 34, [Available from World Meteorological Organization, Case Postale 2300, CH-1211 Geneva 2, Switzerland.]

Almut, G. and *Herzog, H.J.,* 2007: A consistent time-split numerical scheme applied to the nonhydrostatic compressible equations. *Mon. Weather Rev. 135*, 20–36.

Andre, J.C., DeMoor, G., Lacarrere, P., Therry, G., and *Du Vachat, R.,* 1978: Modelling the 24-hour evolution of the mean and turbulent structures of the planetary boundary layer. *J Atmos Sci 35*, 1861–1883.

ANSYS Inc., 2012: FLUENT 13 documentation. In: Fluent User Services Center. [Available online at http://www.fluentusers.com/fluent/doc/doc_f.htm., Cited 26. September 2012.]

Baklanov, A.A., Grisogono, B., Bornstein, R., Mahrt, L., Zilitinkevich, S.S., Taylor, P., Larsen, S.E., Rotach, M.W., and *Fernando, H.J.S.,* 2011: The nature, theory, and modeling of atmospheric planetary boundary layers. *B. Am. Meteorol. Soc. 92*, 123–128.

Balczó, M., Balogh, M., Goricsán, I., Nagel, T., Suda, J.M., and *Lajos, T.,* 2011: Air quality around motorway tunnels in complex terrain - Computational Fluid Dynamics modeling and comparison to wind tunnel data. *Időjárás 115,* 179–204.

Balogh, M. and Krisróf, G., 2010: Fine scale simulation of turbulent flows in urban canopy layers. *Időjárás 114*, 135–148.

Belušič, D. and *Klaič, Z.B.,* 2004: Estimation of bora wind gusts using a limited area model. *Tellus A 56*, 296–307.

Berg, L.K. and *Zhong, S.,* 2005: Sensitivity of MM5-Simulated Boundary Layer Characteristics to Turbulence Parameterizations. *J. Appl. Meteorol.* 44, 1467–1483.

Blackadar, A.K., 1976: Modeling the nocturnal boundary layer. Preprints of the Third Symposium on Atmospheric Turbulence and Air Quality, Rayleigh, NC, 19–22 October 1976, Amer. Meteor. Soc., Boston, 46–49.

Blocken, B., Stathopoulos, T. and *Carmeliet, J.,* 2007: CFD simulation of the atmospheric boundary layer: wall function problems. *Atmos. Environ. 41*, 238–252.

Brinkman, W.A.R., 1974: Strong downslope winds at Boulder, Colorado. *Mon. Weather Rev. 102*, 592–602.

Castro, F.A., Santos, C.S. and *Palma, J.M.L.M.,* 2008: Parallelisation of the CFD Code of a CFD-NWP Coupled System for the Simulation of Atmospheric Flows over Complex Terrain. *High Performance Computing for Computational Science - VECPAR* 2008, 27–38.

Cenedese, A. and *Monti, P.,* 2003: Interaction between an urban heat island and a sea-breeze flow. A laboratory study. *J. Appl. Meteorol. 42*, 1569–1583.

Chang, J.C. and *Hanna, S.R.,* 2004: Air quality model performance evaluation. *Meteorol. Atmos. Phys. 87*, 167–196.

Chang, J.C., Hanna, S.R., Boybeyi, Z. and *Franzese, P.,* 2005: Use of Salt Lake City URBAN 2000 Field Data to Evaluate the Urban Hazard Prediction Assessment Capability (HPAC) Dispersion Model. *J. Appl. Meteorol. 44*, 485–501.

Colle, B.A. and *Mass, C.F.,* 2000: High resolution observation and numerical simulation of easterly gap flow through the strait of Juan de Fuca on 9–10 December 1995. *Mon. Weather Rev. 128,* 2398–2422.

Corrsin, S., 1975: Limitation of gradient transport models in random walks and in turbulence. *Adv. Geophys. 18A*, 25–60.

Deardorff, J.W., 1974a: Three-dimensional numerical study of the height and mean structure of a heated planetary boundary layer. *Bound.-Lay. Meteorol. 7*, 81–106.

Deardorff, J.W., 1974b: Three-dimensional numerical study of turbulence in an entraining mixed layer. *Bound.-Lay. Meteorol. 7*, 199–226.

Deardorff, J.W., 1980: Stratocumulus-capped mixed layers derived from a three-dimensional model. *Bound.-Lay. Meteorol. 18*, 495–527.

Doyle, J.D., Durran, D.R., Chen, C., Colle, B.A., Georgelin, M., Grubisic, V., Hsu, W.R., Huang ,C.Y., Landau, D., Lin, Y.L., Poulus, G.S., Sun, W.Y., Weber, D.B., Wurtele, M.G., and *Xue, M.,* 2000: An intercomparison of model-predicted wave breaking for the 11 January 1972 boulder windstorm. *Mon. Weather. Rev. 128*, 901–914.

Doyle, J.D. and *Durran, D.R.,* 2002: The Dynamics of mountain–wave induced rotors. *J. Atmos. Sci. 59,* 186–201.

Dudhia, J., 1993: A nonhydrostatic version of the Penn State / NCAR mesoscale model: Validation tests and simulations of an Atlantic cyclone and cold front. *Mon. Weather Rev. 121*, 1493–1513.

Durran, D.R. and *Klemp, J.B.,* 1983: A Compressible model for the simulation of moist mountain waves. *Mon. Weather. Rev 111*, 2341–2361.

Durran, D.R., 1986: Another look at downslope windstorms. Part I: The development of analogs to supercritical flow in an infinitely deep, continuously stratified fluid. *J. Atmos. Sci. 43*, 2527–2543.

Durran, D.R., 1990: Mountain waves and downslope winds. Atmospheric Processes over Complex Terrain. *Meteorol. Monog. 45*, 59–81.

Duynkerke, P.G., 1988: Application of the E–ε turbulence closure model to the neutral and stable atmospheric boundary layer. *J. Atmos. Sci. 45*, 865–880.

Faragó, I., 2006: Application of the operator splitting method for real-life problems. *Időjárás 110*, 379-395.

Freedman, F.R. and Jacobson, M.Z., 2003: Modification of the Standard ε equation for the stable ABL through enforced consistency with Monin-Obukhov similarity theory. *Bound-Lay Meteorol* 106, 384–410.

Gatski, T.B. and *Jongen, T.,* 2000: Nonlinear eddy viscosity and algebraic stress models for solving complex turbulent flows. *Prog. Aerosp. Sci. 36*, 655–682.

Geiser, J., 2008: Iterative operator-splitting methods with higher-order time integration methods and applications for parabolic partial differential equations. *J. Comput. Appl. Math. 217*, 227–242.

Grell, G.A., Dudhia, J. and *Stauffier, D.R.,* 1995: A description of the fifth-generation Penn State/NCAR mesoscale model. *NCAR Tech. Note, NCAR/TN-398-398+ST.*

Gyüre, B. and *Jánosi, I.M.*, 2003: Stratified flow over asymmetric and double bell-shaped obstacles. *Dynam. Atmo.s Oceans 37*, 155–170.

Hanjalic, K. and *Launder, B.E.*, 1972: A Reynolds stress model of turbulence and its application to thin shear flows. *J. Fluid Mech. 52*, 609–638.

Hanna, S.R., Strimaitis, D.G. and *Chang, J.C.*, 1991: Evaluation of commonly-used hazardous gas dispersion models. Vol. II, Hazard Response Modeling Uncertainty (A Quantitative Method). *Rep. A119/A120 prepared by Earth Tech, Inc., for Engineering and Services Laboratory, Air Force Engineering and Services Center, and for the American Petroleum Institute,* 334 pp.

Hanna, S.R., Chang, J.C. and *Strimaitis, D.G.*, 1993: Hazardous gas model evaluation with field observations. *Atmos. Environ.* 27A, 2265–2285.

Hanna, S.R., Brown, M.J., Camelli, F.E., Chan, S.T., Coirier, W.J., Kim, S. and *Reynolds, R.M.*, 2006: Detailed Simulations of Atmospheric Flow and Dispersion in Downtown Manhattan: An Application of Five Computational Fluid Dynamics Models. *B. Am. Meteorol. Soc. 87*, 1713–1726.

Hargreaves, D.M. and *Wright, N.G.*, 2007: On the use of the k–ε model in commercial CFD software to model the neutral atmospheric boundary layer. *J. Wind Eng. Ind. Aerod. 95*, 355–369.

Havasi, Á., Bartholy, J., and *Faragó, I.,* 2001: Splitting method and its application in air pollution modeling. *Időjárás 105*, 39–58.

Holton, J.R., 2004: An Introduction to Dynamic Meteorology. 4th Edition, Academic Press, 192–212

Holtslag, A.A.M. and *Moeng, C.-H.,* 1991: Eddy diffusivity and countergradient transport in the convective atmospheric boundary layer. *J. Atmos. Sci. 48*, 1690–1698.

Hong, S.-Y., 2010: A new stable boundary-layer mixing scheme and its impact on the simulated East Asian summer monsoon. *Q. J. Roy. Meteorol. Soc. 136*, 1481–1496.

Hong, S.-Y. and *Pan, H.-L.,* 1996: Nonlocal boundary layer vertical diffusion in a medium-range forecast model. *Mon. Weather Rev. 124*, 2322–2339.

Hong, S.-Y., Noh, Y, and *Dudhia, J.,* 2006: A new vertical diffusion package with an explicit treatment of entrainment processes. *Mon. Weather Rev. 134*, 2318–2341.

Horváth, Á., Geresdi, I., Németh, P. and *Dombai, F.,* 2007: The Constitution Day storm in Budapest: Case study of the August 20, 2006 severe storm. *Időjárás 111*, 41–63.

Huser, A., Nilsen, P.J. and *Skatun, H.,* 1997: Application of k-ε model to the stable ABL: pollution in complex terrain. *J. Wind Eng. Ind. Aerod. 67–68*, 425–436.

Janjic, Z.I., 1990: The step–mountain coordinates: physical package. *Mon. Weather Rev. 118*, 1429–1443.

Janjic, Z.I., 1996: The Mellor-Yamada level 2.5 scheme in the NCEP Eta Model. 11th Conference on Numerical Weather Prediction, Norfolk, VA, 19-23 August 1996; Amer Meteor Soc, Boston, MA, 333–334.

Janjic, Z.I., 2002: Nonsingular Implementation of the Mellor-Yamada Level 2.5 Scheme in the NCEP Meso model. *NCEP Office Note 437.*

Kasahara, A., 1974: Various vertical coordinate systems used for numerical weather prediction. *Mon. Weather Rev. 102*, 509–522.

Klemp, J.B. and *Lilly, D.K.,* 1975: The dynamics of wave-induced downslope winds. *J. Atmos. Sci. 32*, 320–339.

Klemp, J.B. and *Wilhelmson, R.B.,* 1978: The simulation of three-dimensional convective storm dynamics. *J. Atmos. Sci. 35*, 1070–1096.

Klemp, J.B., Skamarock, W.C., and *Dudhia, J.,* 2007: Conservative Split-Explicit Time Integration Methods for the Compressible Nonhydrostatic Equations. *Mon. Weather Rev. 135*, 2897–2913.

Knievel, J.C., Bryan, G.H. and *Hacker, J.P.,* 2007: Explicit Numerical Diffusion in the WRF Model. *Mon. Weather Rev. 135*, 3808–3824.

Kristóf, G., Rácz, N., and *Balogh, M.,* 2009: Adaptation of Pressure Based CFD Solvers for Mesoscale Atmospheric Problems. *Bound.-Lay. Meteorol. 131*, 85–103.

Launder, B.E. and *Spalding, D.B.,* 1972: Lectures in mathematical models of turbulence. Academic Press, London, England 1972. 169 pp.

Lee, S.-M., Giori, W., Princevac, M., and *Fernando, H.J.S.,* 2006: Implementation of a Stable PBL Turbulence Parameterization for the Mesoscale Model MM5: Nocturnal Flow in Complex Terrain. *Bound.-Lay. Meteorol. 119*, 109–134.

Lesieur, M., 2008: Turbulence in Fluids. Fourth edition, Springer, ISBN: 9781402064340.

Lilly, D.K. and *Zipser, E.J.,* 1972: The front range windstorm of 11 January 1972 – a meteorological narrative. *Weatherwise 25*, 56–63.

Lin, Y-L., 2007: Mesoscale dynamics. Cambridge University Press, ISBN 9780521808750.

Long, R.R., 1953: Some aspects of the flow of stratified fluids. I. A theoretical investigation. *Tellus 5*, 42–58.

Lopes da Costa, J.C., Castro, F.A., Palma, J.M.L.M., and *Stuart, P.,* 2006: Computer simulation of atmospheric flows over real forests for wind energy resource evaluation. *J. Wind Eng. Ind. Aerod.* 94, 603–620.

Lu, J., Arya, S.P., Snyder, W.H. and *Lawson Jr., R.E.,* 1997: A laboratory study of the urban heat island in a calm and stably stratified environment. Part I: Temperature field. *J. Appl. Meteorol. 36*, 1377–1391.

Lundquist, J.K. and *Chan, S.T.,* 2006: Consequences of urban stability conditions for computational fluid dynamics simulations of urban dispersion. *J. Appl. Meteorol. Clim. 46*, 1080–1097.

Lynch, P., 2006: The Emergence of Numerical Weather Prediction: Richardson's Dream. Cambridge University Press, Cambridge, ISBN: 0521857295.

Madala, R.V., 1981: Efficient time integration schemes for atmosphere and ocean models. In (Book, D.L. Ed.) Fine-difference techniques for vectorized fluid dynamics calculations. Springer-Verlag, New York, 56–74.

Manual of the ICAO Standard Atmosphere, 1993: Doc 7488-CD, Third Edition, ISBN: 92-9194-004-6.

Mellor, G.L. and *Yamada, T.,* 1974: A hierarchy of turbulence closure models for planetary boundary layers. *J. Atmos. Sci. 31*, 1791–1806.

Mellor, G.L. and *Yamada, T.,* 1982: Development of a turbulence closure model for geophysical fluid problems. *Rev. Geophys. 20*, 851–875.

Michioka, T. and *Chow, F.K.,* 2008: High-resolution large-eddy simulations of scalar transport in atmospheric boundary layer flow over complex terrain. *J. Appl. Meteorol. Climatol. 47*, 3150–3169.

Montavon C., 1998: Simulation of atmospheric flow over complex terrain for wind power potential assessment. Doctoral thesis, EPFL, Lausanne, doi: 10.5075/epfl-thesis-1855.

Nagy, A., 2010: Application of WRF model for the meso-g scale processes. MSc Thesis Eötvös Loránd University, Departmernt of Meteorology. (In Hungarian)

Nakanishi, M. and *Niino, H.,* 2009: Development of an Improved Turbulence Closure Model for the Atmospheric Boundary Layer. *J. Meteorol. Soc. JPN* 87, 895–912.

National Research Council, 1983. Low-Altitude Wind Shear and Its Hazard to Aviation. Washington, DC: The National Academies Press, Washington, DC, 1. Print.

Noto, K., 1996: Dependence of heat-island phenomena on stable stratification and heat quantity in a calm environment. *Atmos. Environ. 30*, 475–485.

Palma, J.M.L.M., Castro, F.A., Ribeiro, L.F., Rodrigues, A.H.. and *Pintod, A.P.,* 2008: Linear and nonlinear models in wind resource assessment and wind turbine micro-siting in complex terrain. *J. Wind Eng. Ind. Aerod.* 96, 2308–2326.

Peltier, W.R. and *Clark, T.L.,* 1979: The evolution and stability of finite-amplitude mountain waves. Part II: Surface wave drag and severe downslope windstorms. *J. Atmos. Sci. 36*, 1498–1529.

Pleim, J.E., 2007: A combined local and nonlocal closure model for the atmospheric boundary layer. Part II: Application and evaluation in a mesoscale meteorological model. *J. Appl. Meteorol. Climatol. 46*, 1396–1409.

Pleim, J.E. and *Chang, J.S.,* 1992: A non-local closure model for vertical mixing in the convective boundary layer. *Atmos. Environ. 26A*, 965–981.

Pontiggia, M., Derudi, M., Busini, V., and *Rota, R.,* 2009: Hazardous gas dispersion: A CFD model accounting for atmospheric stability classes. *J. Hazard Mater. 171*, 739–747.

Qiu, X.-L. and Xia, K.-Q., 1998: Viscous boundary layers at the sidewall of a convection cell. *Phys. Rev. E 58*, 486–491.

Richard, E., Mascart, P. and *Nickerson, E.C.,* 1989: The role of surface friction in downslope wind storms. *J. Appl. Meteorol. 28*, 241–251.

Richards, P.J. and *Hoxey, R.P.,* 1993: Appropriate boundary conditions for computational wind engineering models using the k–ε turbulence model. *J. Wind Eng. Ind. Aerod. 46–47*, 145–153.

Saito, K., Ishida, J., Aranami, K., Hara, T., Segawa, T., Narita, M., and *Honda, Y.,* 2007: Nonhydrostatic atmospheric models and operational development at JMA. *J. Meteorol. Soc. JPN 85B*, 271–304.

Schumann, U., Hauf, T., Holler, H., Schmidt, H,. and *Volkert, H.,* 1987: A mesoscale model for the simulation of turbulence, clouds and flow over mountains: Formulation and validation examples. *Beitr. Phys. Atmos. 60*, 413–446.

Scorer, R.S., 1949: Theory of waves in the lee of mountains. *Q. J. Roy. Meteor. Soc.* 75, 41–56.

Shafran, P.C., Seaman, N.L., and *Gayno, G.A.,* 2000: Evaluation of numerical predictions of boundary layer structure during the Lake Michigan Ozone Study (LMOS). *J. Appl. Meteorol. 39* 412–426.

Shih, T.-H., Liou, W.W., Shabbir, A., Yang, Z., and *Zhu, J.,* 1995: A new k–ε eddy-viscosity model for high Reynolds number turbulent flows – model development and validation. *Comput. Fluids 24*, 227–238.

Simon, A., Horváth, Á., and *Vivoda, J.,* 2006: Case study and numerical simulations of the November 19, 2004 severe windstorm in central Europe. *Időjárás 110*, 91–123.

Skamarock, W.C., Klemp, J.B., Dudhia, J., Gill, D.O., Barker, D.M., Wang, W., and *Powers, J.G.,* 2005: A Description of the Advanced Research WRF Version 2. *NCAR/TN–468+STR NCAR Technical Note*.

Smith, R.B., 1979: The influence of mountains on the atmosphere. Adv Geophys, Academic Press 21, 87–230.

Smith, R.B., 2002: Stratified airflow over mountains. In (Grimshaw, R., Ed.) Environmental Stratified Flows, Kluwer Publishing, 119–159.

Smith, R.B., Skubis, S., Doyle, J.D., Broad, A.S., Kiemle, C. and *Volkert, H.*, 2002: Mountain waves over Mont Blanc: Influence of stagnant boundary layer. *J. Atmos. Sci. 59*, 2073–2092.

Stull, R.B., 1993: Review of non-local mixing in turbulent atmospheres: Transilient turbulence theory. *Bound.-Lay. Meteorol. 62*, 21–96.

Sušelj, K. and *Sood, A,* 2010: Improving the Mellor–Yamada–Janjic parameterization for wind conditions in the marine planetary boundary layer. *Bound.-Lay. Meteorol. 136*, 301–324

Thunis, P. and *Clappier, A.,* 2000: Formulation and evaluation of a Nonhydrostatic Mesoscale Vorticity Model (TVM). *Mon. Weather Rev. 128*, 3236–3251.

Townsend, A.A., 1980: The response of sheared turbulence to additional distortion. *J. Fluid. Mech. 98*, 171–191.

Troen, I. and *Mahrt, L.,* 1986: A simple model of the atmospheric boundary layer; sensitivity to surface evaporation. *Bound.-Lay. Meteorol. 37*, 129–148.

Vendel, F., Lamaison, G., Soulhac, L., Volta, P., Donnat, L., Duclaux, O., and *Puel, C.,* 2010: Modelling diabatic atmospheric boundary layer using a RANS CFD code with k-epsilon turbulence closure. *HARMO13 – 1–4 June 2010, Paris, France – 13th Conference on Harmonisation within Atmospheric Dispersion Modelling for Regulatory Purposes* H13-124, 652–656.

Voisin, B., 1994: Internal wave generation in uniformly stratified fluids. Part 2. Moving point sources. *J. Fluid. Mech. 261*, 333–374.

Weigel, A.P., Chow, F.K., and *Rotach, M.W.,* 2007: On the nature of turbulent kinetic energy in a steep and narrow Alpine valley. *Bound.-Lay. Meteorol. 123*, 177–199.

Wicker, L.J. and *Skamarock, W.C.,* 2002: Time splitting methods for elastic models using forward time schemes. *Mon. Weather Rev. 130*, 2088–2097.

Wilhelmson, R. and *Klemp, J.B.,* 1978: A numerical study of storm splitting that leads to long-lived storms. *J. Atmos. Sci. 35*, 1974–1986.

Williams, M.D., Brown, M.J., Singh, B., and *Boswell, D.,* 2004: QUIC-Plume Theory Guide. LANL Report: LA-UR-04-0561.

Wyngaard, J.C., Cote, O.R., and *Rao, K.S.,* 1974: Modeling of the atmospheric boundary layer. *Adv. Geophys. 18(A),* 193–212.

Wyngaard, J.C. and *Brost, R.A.,* 1984: Top-down and bottom-up diffusion of a scalar in the convective boundary layer. *J. Atmos. Sci. 41*, 102–112.

Wurtele, M.G., Sharman, R.D., and *Datta, A.,* 1996: Atmospheric lee waves. *Annu. Rev. Fluid. Mech. 28*, 429–476.

Xue, M., Zong, J., and *Drogemeier, K.K.,* 1996: Parameterization of PBL turbulence in a multi-scale nonhydrostatic model. Preprints, 11th Conf. on Numerical Weather Prediction, Norfolk, VA, Amer Meteor Soc, P2.5.

Xue, M., *Droegemeier, K.K.,* and *Wong, V.,* 2000: The Advanced Regional Prediction System (ARPS). A multi-scale nonhydrostatic atmospheric simulation and prediction model. Part I: Model dynamics and verification. *Meteorol. Atmos. Phys. 75*, 161–193.

Yang, X., 1993: A nonhydrostatic model for simulation of airflow over mesoscale bell-shaped ridges. *Bound.-Lay. Meteorol*. 65, 401–424.

Zhang, D.-L. and *Anthes, R.A.,* 1982: A high-resolution model of the planetary boundary layer-sensitivity tests and comparisons with SESAME-79 data. *J. Appl. Meteorol*. 21, 1594–1609.

Zhong, S., In, H., and *Clements, C.,* 2007: Impact of turbulence, land surface, and radiation parameterizations on simulated boundary layer properties in a coastal environment. *J. Geophys. Res. 112*, D13110, doi:10.1029/2006JD008274.

Zilitinkevich, S.S., 1995: Non-local turbulent transport: pollution dispersion aspects of coherent structure of convective flows. In (Power, H., Moussiopoulos, N., and Brebbia, C.A., Eds.) Air Pollution III—Volume I. Air Pollution Theory and Simulation, Computational Mechanics Publications, Southampton Boston, 53–60.